Receptivity of crossflow-dominated boundary layers

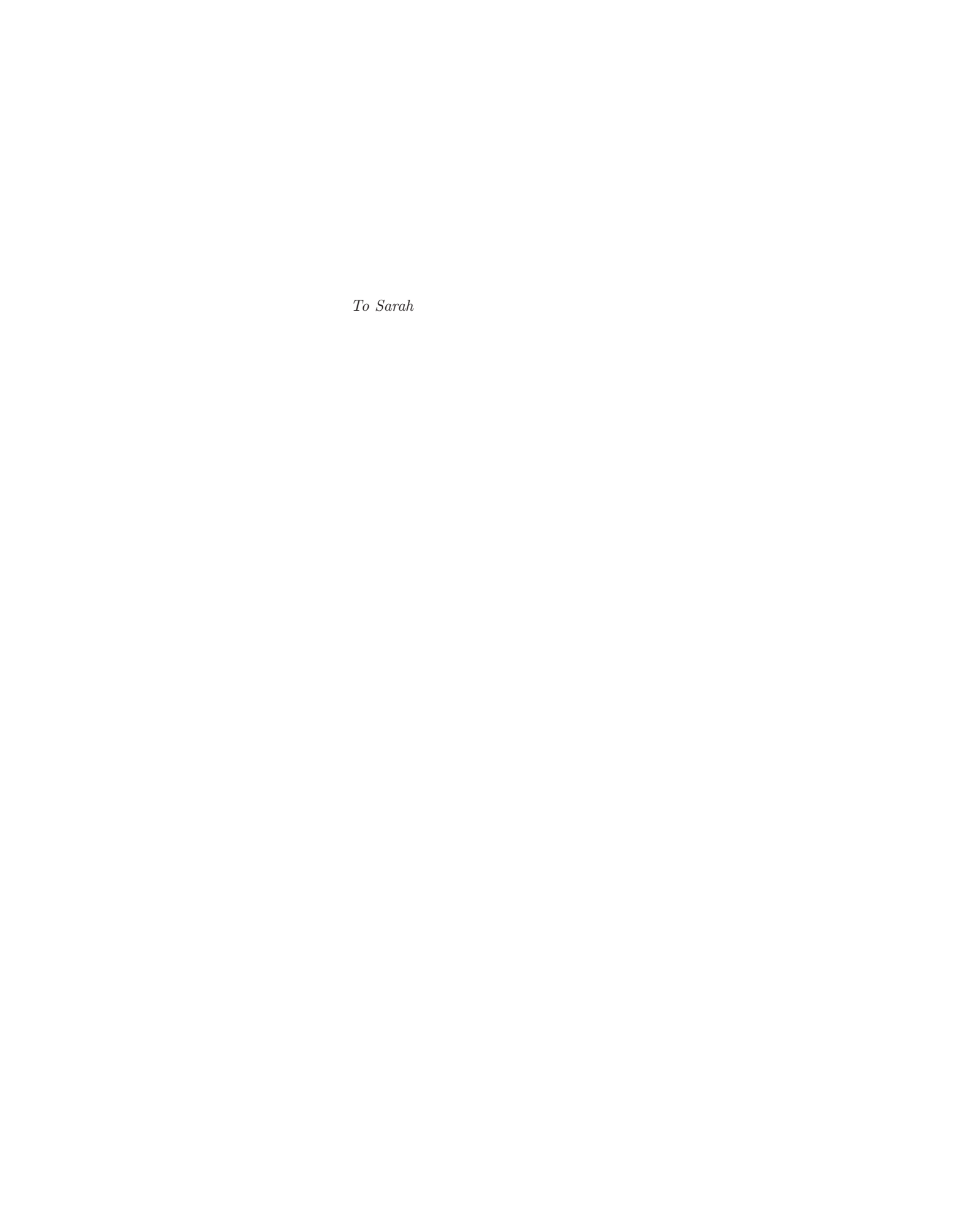
by

David Tempelmann

December 2011 Technical Reports Royal Institute of Technology Department of Mechanics SE-100 44 Stockholm, Sweden

Akademisk avhandling som med tillstånd av Kungliga Tekniska Högskolan i Stockholm framlägges till offentlig granskning för avläggande av teknologie doktorsexamen fredagen den 9:e december 2011 kl 10.15 i sal F3 vid Kungliga Tekniska Högskolan, Lindstedtsvägen 26, Stockholm.

©David Tempelmann 2011 Universitetsservice US-AB, Stockholm 2011



Receptivity of crossflow-dominated boundary layers

David Tempelmann

Linné FLOW Centre, KTH Mechanics, Royal Institute of Technology SE-100 44 Stockholm, Sweden

Abstract

This thesis deals with receptivity mechanisms of three-dimensional, crossflow-dominated boundary layers. The receptivity of two model problems, a swept-flat-plate and a swept-wing boundary layer, is investigated by solving the parabolised stability equations (PSE) as well as by performing direct numerical simulations (DNS). Both flow cases are known to exhibit strong inflectional instabilities, the crossflow disturbances, whose excitation by external disturbances such as surface roughness or free-stream vorticity is studied. One focus is on worst-case scenarios. This involves the determination of optimal conditions, i.e. those disturbance environments yielding the largest possible response inside the boundary layer.

A new method on the basis of the PSE is presented which allows to study optimal disturbances of swept-flat-plate boundary layers. These take the form of tilted streamwise vortices. While convected downstream they develop into streamwise streaks experiencing strong non-modal growth. Eventually, they turn into crossflow disturbances and undergo exponential growth. Non-modal growth is thus found to optimally excite crossflow disturbances and can be related to a receptivity mechanism of three-dimensional boundary layers. Evaluating effects of compressibility reveals that the potential for both non-modal and modal growth increases for higher Mach numbers. It is shown that wall cooling has diverse effects on disturbances of non-modal and modal nature. While destabilising the former it attenuates the growth of modal disturbances. Concave curvature on the other hand is found to be equally destabilising for both types of disturbances.

The adjoint of the linearised Navier-Stokes equations is solved for a swept-wing boundary layer by means of DNS. The adjoint solution of a steady cross-flow disturbance is computed in the boundary layer as well as in the free-stream upstream of the leading edge. This allows to determine receptivity to incoming free-stream disturbances and surface roughness as well as the corresponding worst-case scenarios. Upstream of a swept wing the optimal initial free-stream disturbance is found to be of streak-type which convects downstream towards the leading edge. It entrains the boundary layer a short distance downstream of the stagnation line. While minor streamwise vorticity is present the streak component is dominant all the way into the boundary layer where the optimal disturbance turns into a crossflow mode. Futher, the worst-case surface roughness is determined. It takes a wavy shape and is distributed in the chordwise direction. It is shown that, under such optimal conditions, the swept-wing

boundary layer is more receptive to surface roughness than to free-stream disturbances.

Another focus of this work has been the development and evaluation of tools for receptivity prediction. Both DNS and direct and adjoint solutions of the PSE are used to predict the receptivity of a swept-wing boundary layer to localised surface roughness. The configuration conforms to wind tunnel experiments performed by Saric and coworkers at the Arizona State University. Both the DNS and the PSE are found to predict receptivity amplitudes which are in excellent agreement with each other. Though the predicted disturbance amplitudes are slightly lower than experimental measurements the overall agreement with experimental results is very satisfactory.

Finally, a DNS of the stabilisation of a transitional swept-wing boundary layer by means of discrete roughness elements is presented. This control approach is found to completely suppress transition to turbulence within the domain studied and confirms experimental results by Saric & coworkers.

Descriptors: Receptivity, crossflow instability, optimal disturbances, non-modal growth, three-dimensional boundary layer, swept-wing flow, parabolised stability equations, adjoint solutions

V

Preface

This thesis in fluid mechanics consists of two parts. The first part is written as an introduction into stability characteristics and receptivity mechanisms of three-dimensional, crossflow-dominated boundary layers. Using the example of a swept-flat-plate boundary layer all methods that have been employed throughout this work are introduced in an illustrative manner. The second part contains the following papers. These are presented in the published or submitted form except for minor corrections.

- **Paper 1.** D. Tempelmann, A. Hanifi & D. S. Henningson, 2010 Spatial optimal growth in three-dimensional boundary layers. *J. Fluid Mech.* **646**, 5–37.
- **Paper 2.** D. Tempelmann, A. Hanifi & D. S. Henningson, 2011 Spatial optimal growth in three-dimensional compressible boundary layers. *Submitted to J. Fluid Mech.*
- Paper 3. D. Tempelmann, L.-U. Schrader, A. Hanifi, L. Brandt & D. S. Henningson, 2011 Swept-wing boundary-layer receptivity to localised surface roughness. Submitted to J. Fluid Mech.
- **Paper 4.** D. Tempelmann, A. Hanifi & D. S. Henningson, 2011 Sweptwing boundary-layer receptivity. *Submitted to J. Fluid Mech.*
- **Paper 5.** D. Tempelmann, S. M. Hosseini, A. Hanifi & D. S. Henningson, 2011 Stabilisation of a swept-wing boundary layer by localised surface roughness. $Internal\ report$

The following papers, though related, have not been included into this thesis.

- D. Tempelmann, A. Hanifi & D. S. Henningson, 2009 Spatial Optimal Disturbances in Three-Dimensional Boundary Layers. In *Proceedings of the 7th IUTAM symposium on Laminar-Turbulent Transition, Stockholm, Sweden* (ed. D. S. Henningson & P. Schlatter).
- D. TEMPELMANN, A. HANIFI & D. S. HENNINGSON, 2009 Receptivity to Free-Stream Disturbances in Three-Dimensional Boundary Layers. *Final report of the European TELFONA project*. In D. Tempelmann 2009, Licentiate Thesis, TRITA-MEK 2009:19.
- D. TEMPELMANN, A. HANIFI & D. S. HENNINGSON, 2009 Receptivity to Roughness in Three-Dimensional Boundary Layers. *Final report of the European TELFONA project*. In D. Tempelmann 2009, Licentiate Thesis, TRITA-MEK 2009:19.
- D. Tempelmann, A. Hanifi & D. S. Henningson, 2010 Optimal disturbances and receptivity in three-dimensional boundary layers. In *Proceedings of the 5th European Conference on Computational Fluid Dynamics ECCOMAS CFD* (ed. J.C.F. Pereira & A. Sequeira).
- D. Tempelmann, L.-U. Schrader, A. Hanifi, L. Brandt & D. S. Henningson, 2011 Numerical studies on swept-wing boundary layer receptivity. *AIAA Paper 2011-3294*.
- L.-U. Schrader, D. Tempelmann, L. Brandt, A. Hanifi & D. S. Henningson, 2011 Excitation of cross-flow vortices by surface roughness on a swept wing. In *Proceedings of the CASI AERO 2011 conference, Montreal, Canada.*
- D. Tempelmann, L.-U. Schrader, A. Hanifi, L. Brandt & D. S. Henningson, 2011 Modelling roughness and receptivity in three-dimensional boundary layers. In *Proceedings of the 7th International Symposium on Turbulence and Shear Flow Phenomena, TSFP, Ottawa, Canada.*

Division of work between authors

The research project was initiated by Adj. Prof. Ardeshir Hanifi (AH) and Prof. Dan Henningson (DH) who have been supervising this work.

Paper 1

The code development as well as the computations were performed by David Tempelmann (DT) with input from AH. The paper was written by DT with feedback from AH and DH.

Paper 2

Development of the codes as well as simulations were performed by DT with feedback from AH. The paper was written by DT with feedback from AH and DH.

Paper 3

The initial simulations have been set up by DT and Dr. Lars-Uve Schrader (LS). The PSE codes have been developed by DT. The final simulations were run by DT using the open-source spectral element code 'Nek5000'. Complementary RANS simulations were performed by AH. The paper was written by DT and LS with feedback from AH, Dr. Luca Brandt and DH.

Paper 4

Simulations using 'Nek5000' and receptivity computations were performed by DT. The paper was written by DT with feedback from AH and DH.

Paper 5

The simulation cases were set up by Seyed M. Hosseini (SH) and DT using tools developed by DT. Simulations were run by SH using 'Nek5000'. The data was post-processed by SH with input from DT. The paper was written by DT with input from SH and feedback from AH and DH.

Abstract	iv
Preface	vi
Chapter 1. Introduction	1
Chapter 2. Transition in three-dimensional boundary layers	3
2.1. Three-dimensional boundary layers	3
2.2. Stages of transition	4
2.2.1. Instability mechanisms	4
2.2.2. Receptivity	7
2.2.3. Non-linear effects and breakdown to turbulence	8
Chapter 3. The Falkner–Skan–Cooke Boundary Layer	9
3.1. A reference case	10
Chapter 4. Stability theory	11
4.1. Local stability theory	13
4.1.1. The discrete spectrum - Crossflow mode	14
4.1.2. The continuous spectrum	17
4.2. Nonlocal stability theory	20
4.2.1. Linear PSE	20
4.2.2. Closure & Choice of α	21
4.2.3. Nonlinear PSE	23
4.2.4. PSE results for the FSC boundary layer	24
Chapter 5. Receptivity	28
5.1. Direct receptivity computations	28
5.1.1. Receptivity to surface roughness	28
5.1.2. Receptivity to free-stream disturbances	29
5.2. Receptivity modelling using adjoint solutions	31
5.2.1. Receptivity to surface roughness	34
5.2.2. Receptivity to free-stream disturbances	35
5.2.3. Optimal excitation of modal disturbances	36
5.2.4. Receptivity to spanwise-periodic, time-harmonic sources	38
5.3. Receptivity of a swept-wing boundary layer	40
Chapter 6. Spatial non-modal & optimal growth	44
Chapter 7. Stabilisation by localised roughness	49
Chapter 8. Summary & Conclusions	54

Chapter 9.	Acknowledgements		
Bibliography	y	57	
	Part II - Papers		
Paper 1.	Spatial optimal growth in three-dimensional boundary layers	67	
Paper 2.	Spatial optimal growth in three-dimensional compressible boundary layers	109	
Paper 3.	Swept-wing boundary-layer receptivity to localised surface roughness	141	
Paper 4.	Swept-wing boundary-layer receptivity	175	
Paper 5.	Stabilisation of a swept-wing boundary layer by surface roughness	193	

x

Part I Introduction

CHAPTER 1

Introduction

Reducing carbon dioxide emissions to attenuate global warming is one of the biggest challenges engineers are facing today. Potentials for reduction may be found over a wide range of technical applications. Many of these are, to a greater or lesser extent, connected to fluid mechanics. Increasing the use of natural resources like wind and water for energy production while at the same time reducing the use of fossil fuels constitutes one example. A major potential however, is to significantly increase the efficiency of those technical applications which exist and are in use already today. In particular the transport sector which is responsible for a great part of carbon dioxide emissions needs to be considered. Aviation plays an important role in this sector and the work presented in this thesis is related to the efforts of improving aircraft efficiency.

A large part (about 20 %) of the aerodynamic drag of modern airplanes is attributed to skin friction acting on the wing surface. Skin friction originates from a thin flow layer around solid bodies where viscosity plays an important, non-negligible role. This thin region is known as the boundary layer and its concept was introduced by Ludwig Prandtl in 1904. Boundary layers are known to adopt two principally different flow states. Laminar boundary layers are characterised by a smooth and well ordered flow while chaotic and random fluid motion governs turbulent boundary layers. The transition from laminar to turbulent flow is accompanied by a strong increase in skin friction.

One approach to increase aircraft efficiency is thus to reduce the aerodynamic drag of airplanes through the use of so-called natural laminar flow wings. Since surface friction is significantly increased in turbulent flow the profiles of such wings are chosen so as to obtain laminar flow over the largest possible area of the wing. In order to design wings optimised for these needs engineers require tools which reliably predict aircraft performance and accordingly the onset of transition from laminar to turbulent flow. Other approaches involve the use of passive or active control attenuating the growth of dominant disturbances in order to shift the transition location further downstream. Either approach requires an understanding of the fundamental mechanisms leading to transition.

The aim of the work presented in this thesis has been both to develop a better understanding of transition mechanisms and to develop efficient tools for

1

2 1. INTRODUCTION

transition prediction. The focus is on boundary layers which are characteristic for swept-wing flows.

CHAPTER 2

Transition in three-dimensional boundary layers

2.1. Three-dimensional boundary layers

Modern aircraft are usually equipped with swept-wing configurations. Boundary layers developing on swept wings are principally different from their twodimensional counterparts in that they exhibit a crossflow profile. This crossflow profile results from the combined effect of pressure gradient and sweep angle which leads to a curved streamline in the outer inviscid flow. Inside the boundary layer the pressure gradient remains constant while the streamwise velocity reduces to zero at the wall. This leads to an imbalance of centrifugal and pressure forces which in turn creates a crossflow inside the boundary layer towards the concave side of the external streamline. Such a crossflow profile is illustrated in figure 2.1. It has important implications on boundary-layer stability as will become clear in §2.2.1. Two model problems have been investigated in this thesis, a swept-flat-plate boundary layer and the boundary layer forming on an infinite swept wing. Both cases represent good models for generic sweptwing flows since they comprise the effect of a pressure gradient as well as a sweep angle causing the crossflow profile. Hence, they allow detailed studies of the effect of crossflow on stability and transition.

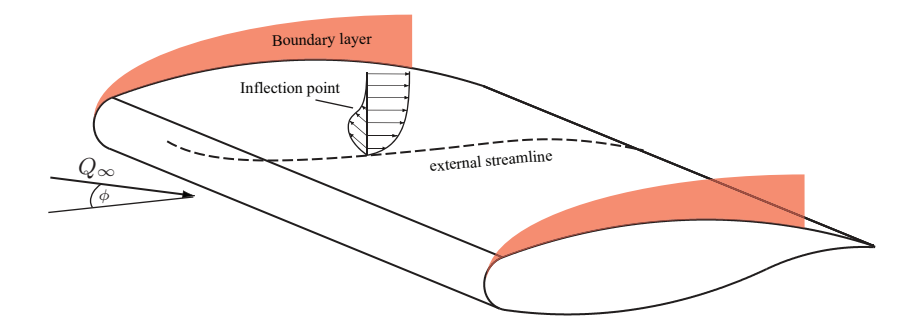


FIGURE 2.1. Illustration of a three-dimensional boundary layer forming on a swept wing which is invariant in the spanwise direction. Q_{∞} denotes the total incoming velocity and ϕ is the sweep angle.



FIGURE 2.2. The basic stages of laminar-turbulent transition in a swept-flat-plate boundary layer. Courtesy of Schrader *et al.* (2010*a*).

2.2. Stages of transition

An instructive illustration of the main stages of transition from laminar to turbulent flow of a swept flat plate boundary layer subject to a favourable pressure gradient is given by Schrader et al. (2010a) (see figure 2.2). The first stage of transition is characterised by external disturbances penetrating the boundary layer. Free-stream turbulence, surface roughness or acoustic disturbances represent such external disturbances. These are filtered by the boundary layer which results in the emergence of instability waves inside the boundary layer. This process is referred to as receptivity. Depending on the disturbance environment various disturbance, exhibiting different time and length scales, are excited in the receptivity stage. While evolving downstream, some become unstable and grow while others decay. Initially this spatial evolution may often be described by linear theory. At some position though, the disturbance amplitudes become sufficiently large to interact non-linearly. This leads to a redistribution of energy among the disturbances and may eventually result in a complex flow state involving amplitude saturation. At this stage the boundary layer becomes unstable to so-called secondary instabilities which evolve on top of the primary ones. These secondary instabilities exhibit high frequencies and rapidly lead to a break-down from laminar to turbulent flow. This break-down stage is led in by the emergence of localised regions of turbulent flow, the turbulent spots, which are nicely depicted in figure 2.2. Eventually, these spots grow in size, merge and lead to a fully turbulent flow. The breakdown stage is accompanied by a strong increase of skin friction.

These main stages are shared among various types of boundary layers exposed to different external disturbance environments. However, the specific receptivity and instability mechanisms dominating the transition process may differ strongly. In the following those mechanisms are introduced which have been found to dominate swept-wing boundary-layer transition.

2.2.1. Instability mechanisms

Several instability mechanisms have been identified in swept-wing boundary layers. Each of these instabilities is characteristic for specific conditions. On

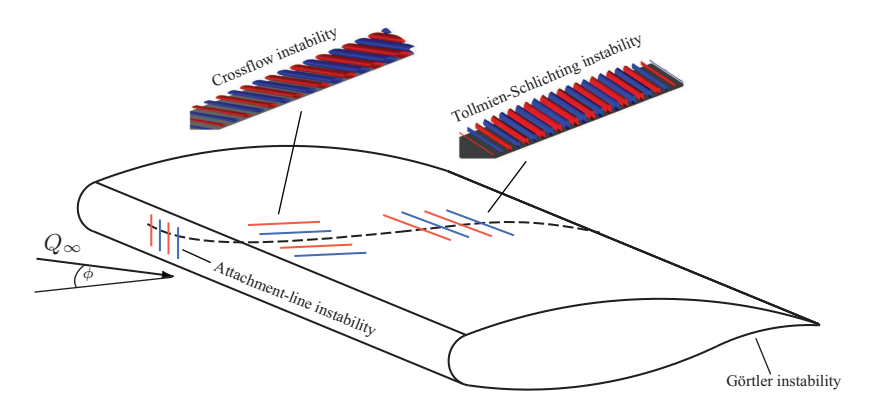


FIGURE 2.3. Illustration of instability mechanisms that are characteristic for three-dimensional swept-wing boundary layers. (Red: positive velocities, Blue: negative velocities)

swept wings such conditions are related to different regions where the boundary layer is governed by effects such as surface curvature or acceleration. Figure 2.3 illustrates instability mechanisms and the respective characteristic regions on a swept wing. The following list represents a brief description of each instability mechanism. Comprehensive reviews are provided by Bippes (1999); Arnal & Casalis (2000) and Saric et al. (2003). Note, however, that realistic disturbance fields may consist of a superposition of several types of instabilities.

Crossflow disturbances develop in three-dimensional boundary layers, e.g. on swept wings and rotating disks, because of a crossflow profile. The latter is an exclusive feature of three-dimensional boundary layers (cf. §2.1). Since the crossflow tends to zero in the free-stream its profile exhibits an inflection point. Rayleigh (1880) found such an inflection point to be a necessary condition for inviscid instabilities to arise. In the case of three-dimensional boundary layers it gives rise to the crossflow instability. Crossflow disturbances therefore represent an instability of inviscid type. They were first identified theoretically by Gregory et al. (1955). Early experimental work revealed that crossflow disturbances appear as boundary layer streaks closely aligned with the external streamline (a brief review is given by Mack 1984). Hence, their lines of constant phase are approximately parallel with the external streamline (see figure 2.3). They exist as both, stationary and travelling waves and are destabilised in boundary layers subject to negative pressure gradients and concave surface curvature. It should be noted that crossflow instabilities appear as co-rotating vortices when presented superposed on to the meanflow and are thus commonly referred to as crossflow vortices. However, the disturbance itself takes the form of counter-rotating vortices while the

dominant velocity component is in the streamwise direction. Some nice experimental visualisations of the crossflow instability are given in Bippes (1999).

Tollmien-Schlichting (TS) waves were first predicted to exist theoretically by Tollmien (1929) and Schlichting (1933) for the Blasius boundary layer. Experimentally they were observed first by Schubauer & Skramstad (1947). TS disturbances are travelling waves and represent a viscous instability (i.e. they are stable in the inviscid limit). These waves also exist in a swept-wing boundary layer where they are sometimes called streamwise instabilities. The latter expression results from the fact that the line of constant phase of TS waves is approximately perpendicular to the external streamline. Hence, the wave vector and the direction of propagation are closely aligned with the streamline direction (cf. figure 2.3). Negative pressure gradients stabilise TS waves while positive pressure gradients have a destabilising effect.

Görtler vortices are also present in both two- and three-dimensional boundary layers over concave surfaces. For such surfaces centrifugal forces destabilise the flow and lead to a stationary instability in the form of counter-rotating vortices. For three-dimensional boundary layers Hall (1985) found that the Görtler mechanism is unimportant if the sweep angle is large compared with $Re^{-\frac{1}{2}}$ where Re is the Reynolds number of the flow. This is the case for most realistic swept-wing configurations. A review on Görtler vortices, sometimes also called *centrifugal instabilities*, is provided by Saric (1994).

Attachment-line instabilities may be found in the boundary layer forming along the attachment line of a swept wing. Theoretically and numerically this instability mechanism has been studied for the swept Hiemenz flow (see e.g. Hall et al. 1984; Lin & Malik 1996), which represents a common model of the attachment-line boundary layer of a swept wing. These studies show that the least stable instability wave is a two-dimensional travelling wave of Tollmien-Schlichting type. A swept-wing flow can be stabilised with respect to the attachment-line instability by choosing a small leading-edge radius. A connection between attachment-line instabilities and crossflow disturbances was found by Mack et al. (2008) who computed global modes of a compressible boundary layer forming on a swept parabolic leading edge.

Non-modal growth represents an instability mechanism which is principally different from the ones mentioned above. Mathematically, all previously described disturbances can be found as eigenmodes of the governing linear operator. For that reason they are called modal disturbances. A stable boundary layer is governed by exponentially decaying eigenmodes. However, a superposition of various decaying eigenmodes can lead to transient growth representing another instability mechanism in boundary layers. Accordingly such disturbances are referred to as non-modal disturbances. An extensive

discussion on transient growth is given in Schmid & Henningson (2001) and Schmid (2007). Studies on spatial non-modal growth in three-dimensional boundary layers are presented in papers 1 & 2.

Crossflow and the related modal and non-modal disturbances (e.g. crossflow modes) are a specific feature of three-dimensional boundary layers and the work presented herein is entirely related to instabilities and their excitation in crossflow-dominated boundary layers.

2.2.2. Receptivity

The term 'receptivity' denotes the part of the transition process that links external disturbance environments to the excitation of the previously described boundary layer disturbances. This process was devoted a lot of attention in the 80's and 90's after several experiments with three-dimensional boundary layers provided diverse observations with respect to transition scenarios. Careful experiments were carried out by Bippes & coworkers (see e.g. Bippes 1999) and Saric & coworkers (see e.g. Saric et~al. 2003) in order to shed light on the receptivity process in three-dimensional boundary layers and its consequences for transition.

Deyhle & Bippes (1996) performed experimental investigations of a crossflow-dominated three-dimensional boundary layer forming on a swept flat plate. They performed tests on the same model in systematically varied disturbance environments and observed a complex dependence of the flow on the environmental conditions. It was found that travelling crossflow modes, which according to linear theory are less stable than their stationary counterparts, only dominate for turbulence levels Tu > 0.2%. For lower turbulence levels stationary crossflow modes were found to dominate and to lead to transition. Surface roughness was thus identified as a key mechanism for the initiation of stationary crossflow vortices. Further Deyhle & Bippes (1996) found the receptivity to sound to be very weak.

Similar results were obtained by Radeztsky et al. (1999) who studied the transition to turbulence in the boundary layer of a swept wing and the effect of localised surface roughness. These authors found that surface roughness has a strong influence on crossflow-dominated transition in that it leads to a domination of stationary crossflow disturbances. It was observed that the transition location is very sensitive to the roughness position. The most effective roughness location regarding triggering transition was found to be the first location of neutral stability of the excited crossflow mode.

Schrader et al. (2010a) reproduced the experimental results qualitatively for a swept-flat-plate boundary layer by means of large-eddy simulations. Hence, experimental and numerical investigations exemplify the importance of including receptivity into transition prediction models. Without being able to account for the effect of free-stream turbulence on boundary-layer stability, results from wind tunnel tests may be difficult to interpret. This is because the

turbulence level in free-flight is assumed to be significantly lower than in most wind tunnels. Stationary vortices excited by surface irregularities are therefore assumed to dominate in free-flight while travelling disturbances could lead to transition in wind tunnels which exhibit high levels of free-stream turbulence.

2.2.3. Non-linear effects and breakdown to turbulence

Once disturbances have been excited through a receptivity process those being unstable will grow while evolving downstream. As long as disturbance amplitudes are low their spatial evolution can be predicted on the basis of linear theory. However, early onset of nonlinear effects in crossflow dominated three-dimensional boundary layers was observed in several experiments (see e.g. Deyhle & Bippes 1996; Saric et al. 1998b). The streaky nature of steady crossflow disturbances leads to complex flow states which may involve saturation of the primary disturbances and which favour the growth of secondary instabilities. In experiments as well as numerical studies (cf. Deyhle & Bippes 1996; Högberg & Henningson 1998; Wassermann & Kloker 2002, 2003; White & Saric 2005) high-frequency secondary instabilities have been observed to grow strongly prior to transition. Malik et al. (1999) found the growth of these to be correlated with the transition location.

These observations point to the importance of considering receptivity when aiming to predict transition since these determine the initial modal amplitudes and thus the position at which nonlinear effects and subsequent secondary instabilities will set in.

CHAPTER 3

The Falkner-Skan-Cooke Boundary Layer

Swept-flat-plate flows which include the combined effect of a pressure gradient and a sweep angle represent an excellent model problem for studying the receptivity and stability of crossflow-dominated boundary layers. An illustration, outlining the evolution of the external streamline as well as the inflectional crossflow profile is presented in figure 3.1. The depicted coordinate system denoting chordwise (x), wall-normal (y) and spanwise (z) directions is adopted in this introductory part. Under certain conditions a similarity solution to

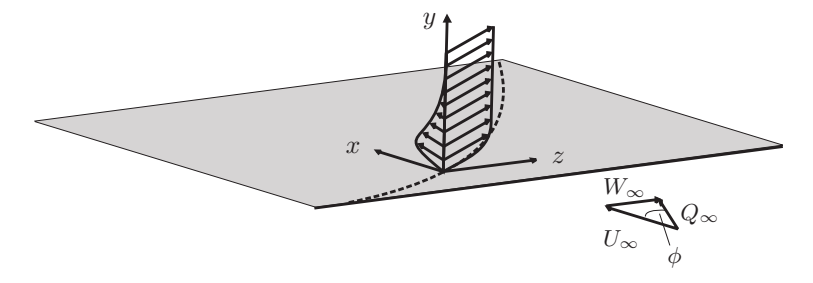


FIGURE 3.1. Illustration of a three-dimensional boundary layer forming above a swept flat plate under pressure gradient which is infinitely elongated in spanwise direction.

the governing boundary layer equations can be found. For incompressible flow these solutions belong to the family of Falkner-Skan-Cooke (FSC) boundary layers (cf. Falkner & Skan 1931; Cooke 1950). For compressible flow no exact similarity solution exists. However, approximate solutions may be obtained and one such example is described in paper 2.

The FSC similarity solution for a swept flat plate boundary layer is obtained by solving the coupled system of ordinary differential equations

$$f''' + ff'' + \beta_H (1 - f'^2) = 0 (3.1a)$$

$$g'' + fg' = 0 (3.1b)$$

if the chordwise and spanwise velocities U_e and W_e of the external inviscid flow obey a power law of the form

$$U_e = \left(\frac{x}{x_n}\right)^m \qquad W_e = U_e(x_n) \tan \phi_n. \tag{3.2}$$

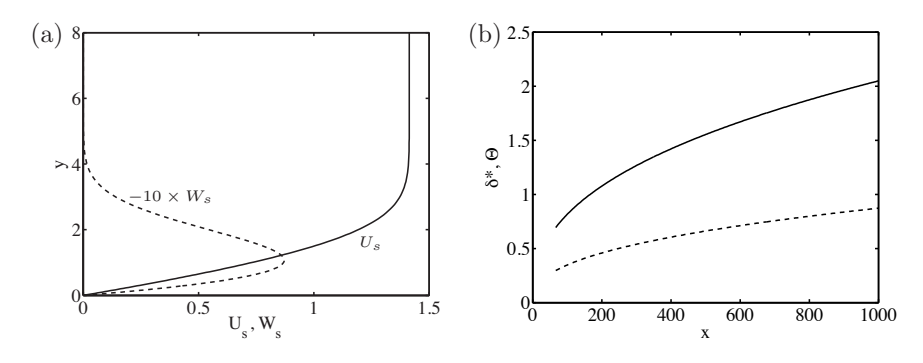


FIGURE 3.2. (a) Boundary layer profiles U_s and W_s projected in the local streamwise and cross-stream direction respectively (denoted by the subscript 's') at $x = x_n = 167$. (b) Displacement thickness δ^* (—) and momentum loss thickness Θ (---) versus chordwise distance x.

Equations (3.1) are solved subject to boundary conditions f = f' = g = 0 at the wall (y = 0) and f' = g = 1 in the free-stream $(y = \infty)$. The subscripts 'e' and 'n' denote the outer inviscid flow and a chosen normalisation position respectively. The sweep angle defined at x_n is denoted ϕ_n . The Hartree parameter β_H is related to m through $m = \beta_H/(2 - \beta_H)$ and determines the pressure gradient. The FSC baseflow profiles are then obtained as

$$U(y) = U_e f'(\eta) \qquad W(y) = W_e g(\eta) \tag{3.3}$$

with $\eta(y)$ being the similarity variable. For a detailed derivation of the FSC similarity solution the reader is referred to Cooke (1950); Schlichting (1979).

3.1. A reference case

The FSC boundary layer shall be used as a reference and example case in the remainder of this introductory part. All stability and receptivity tools presented in the following are employed to the FSC boundary layer studied by Schrader et al. (2009, 2010a). These authors chose a pressure gradient such as to obtain a flow which resembles swept-wing experiments by Reibert (1996). Accordingly, the respective parameters are chosen as $x_n=167$, $\phi(x_n)=45^\circ$ and m=0.2. The Reynolds number is $Re=U_e(x_n)\delta^*(x_n)/\nu=220$. The kinematic viscosity is represented by ν . Note that velocities and lengths will be presented in non-dimensional form in the following based on $U_e(x_n)$ and $\delta^*(x_n)$ respectively. Some boundary layer characteristics as well as streamwise and crossflow velocity profiles are shown in figure 3.2. The crossflow profile shown in figure 3.2(a) clearly exhibits the inflection point mentioned previously which significantly determines the stability characteristics of the underlying boundary layer.

CHAPTER 4

Stability theory

The governing equations of fluid flow are the Navier-Stokes equations which for incompressible flow take the form

$$\frac{\partial \underline{\mathbf{u}}}{\partial t} + (\underline{\mathbf{u}} \cdot \nabla) \underline{\mathbf{u}} = -\nabla \underline{p} + \frac{1}{Re} \nabla^2 \underline{\mathbf{u}}$$

$$\nabla \cdot \underline{\mathbf{u}} = 0.$$
(4.1a)

$$\nabla \cdot \mathbf{u} = 0. \tag{4.1b}$$

Here $\underline{\mathbf{u}} = (\underline{u}, \underline{v}, \underline{w})^T$ represents instantaneous chordwise, wall-normal and spanwise velocity components while p denotes the pressure. All methods presented in this introductory part are introduced for incompressible flow. For a study on optimal growth in compressible flow the reader is referred to paper 2.

When studying receptivity and stability it is the excitation and evolution of perturbations upon a steady baseflow that are of interest. It is thus convenient to decompose the instantaneous velocity and pressure fields $(\underline{\mathbf{u}}, p)$ into a mean (\mathbf{U},P) and a perturbation part (\mathbf{u}',p') such that

$$\underline{\mathbf{u}} = \mathbf{U} + \mathbf{u}' \quad \text{and} \quad p = P + p'.$$
 (4.2)

Both the receptivity process as well as the early evolution phase of perturbations are usually characterised by small amplitude disturbances. It thus makes sense to linearise the NS equations about a steady baseflow. Accordingly, the decomposition (4.2) is introduced into the NS equations. Then the equations governing the steady baseflow are subtracted and products of perturbation quantities are neglected. This yields the linearised Navier-Stokes equations (LNSE) of the form

$$\frac{\partial \mathbf{u}'}{\partial t} + (\mathbf{U} \cdot \nabla) \mathbf{u}' + (\mathbf{u}' \cdot \nabla) \mathbf{U} = -\nabla p' + \frac{1}{Re} \nabla^2 \mathbf{u}' \qquad (4.3a)$$

$$\nabla \cdot \mathbf{u}' = 0. \qquad (4.3b)$$

$$\nabla \cdot \mathbf{u}' = 0. \tag{4.3b}$$

Assuming the baseflow to be invariant in the spanwise direction (which is true for all cases considered in this thesis) perturbations can be represented as Fourier modes of the form

$$\mathbf{q}'(x, y, z, t) = \hat{\mathbf{q}}(x, y)e^{i\beta z - i\omega t} + c.c. \tag{4.4}$$

where $\mathbf{q}' = [u', v', w', p']^T$ denotes the Fourier amplitudes and c.c. represents complex conjugate terms. Further, the LNSE (4.3) are recast in operator form

as

$$\mathcal{L}_s \hat{\mathbf{q}} = 0, \quad \text{with}$$
 (4.5a)

$$\mathcal{L}_s = \mathbf{A} + \mathbf{B} \frac{\partial}{\partial y} + \mathbf{C} \left(\frac{\partial^2}{\partial y^2} + \frac{\partial^2}{\partial x^2} \right) + \mathbf{D} \frac{\partial}{\partial x}.$$
 (4.5b)

The individual operators become

$$\mathbf{A} = \begin{pmatrix} 0 & 0 & i\beta & 0 \\ U_x + \mathcal{Z} & U_y & 0 & 0 \\ V_x & V_y + \mathcal{Z} & 0 & 0 \\ W_x & W_y & \mathcal{Z} & i\beta \end{pmatrix}, \qquad \mathbf{B} = \begin{pmatrix} 0 & 1 & 0 & 0 \\ V & 0 & 0 & 0 \\ 0 & V & 0 & 1 \\ 0 & 0 & V & 0 \end{pmatrix},$$

$$\mathbf{C} = \begin{pmatrix} 0 & 0 & 0 & 0 & 0 \\ -Re^{-1} & 0 & 0 & 0 & 0 \\ 0 & -Re^{-1} & 0 & 0 & 0 \\ 0 & 0 & -Re^{-1} & 0 \end{pmatrix}, \qquad \mathbf{D} = \begin{pmatrix} 1 & 0 & 0 & 0 \\ U & 0 & 0 & 1 \\ 0 & U & 0 & 0 \\ 0 & 0 & U & 0 \end{pmatrix}.$$

$$(4.6b)$$

with $\mathcal{Z} = -i\omega + i\beta W + Re^{-1}\beta^2$.

Solving the system of equations (4.5) for a given steady baseflow (\mathbf{U},P) allows to study its stability by monitoring growth or decay of disturbances. The latter need to be introduced artificially. In the case of boundary layers the perturbations are subject to boundary conditions at the wall and in the free-stream, *i.e.*

$$u = v = w = 0$$
 at $y = 0$ (4.7a)

$$u \to 0, v \to 0, w \to 0$$
 as $y \to \infty$. (4.7b)

Solutions of the LNSE presented in the following have been obtained by using the 'Nek5000' code developed by Fischer $et\ al.\ (2008)$. This code is based on the spectral element method (SEM) which was introduced by Patera (1984). It provides spectral accuracy in space while allowing for the geometrical flexibility of finite element methods. It is therefore well-suited for the study of more complex geometries, e.g. a swept wing, as performed in papers 3, 4 & 5.

Another approach to study stability - not considered in this work - is to reformulate equations (4.5) such as to obtain $i\omega \mathbf{u} = \mathcal{A}\mathbf{u}$ and to compute the eigenvalues ω and eigenmodes of the linear operator \mathcal{A} . These eigenmodes are commonly referred to as global modes and more details on this topic can be found in Theofilis *et al.* (2002); Åkervik *et al.* (2008); Theofilis (2011). Global modes of a swept-wing boundary layer have been computed by Mack *et al.* (2008).

To study the stability of three-dimensional boundary layers both approaches require rather extensive computational resources. However, for certain assumptions the system (4.5) may be simplified, allowing for more efficient solution procedures. Two such approaches are presented in the following. Both are

employed in order to gain insight into the stability characteristics of the FSC boundary layer introduced in §3. In order to evaluate the accuracy and performance of these simplified methods results will be compared to corresponding solutions of the LNSE.

4.1. Local stability theory

Local stability theory is based on the assumption of a locally parallel baseflow. At each position x the baseflow velocities U and W are assumed to be a function of the y-direction only. The variation of the baseflow in the x direction is neglected as is the wall-normal velocity component V. This allows to represent perturbations as Fourier modes in both the z- and the x-direction for spanwise homogeneous baseflows. The corresponding ansatz for the disturbances reads

$$\mathbf{q}'(x, y, z, t) = \mathbf{q}(y)e^{i\alpha x + i\beta z - i\omega t} + c.c., \tag{4.8}$$

where α now represents the chordwise wavenumber and $\hat{\mathbf{q}}(x,y) = \mathbf{q}(y)e^{i\alpha x}$. Introducing (4.8) into (4.3) we obtain the local stability equations (LSE) as

$$\mathcal{L}_l \mathbf{q} = 0, \quad \text{with}$$
 (4.9a)

$$\mathcal{L}_l = \mathbf{A} + \mathbf{B} \frac{\partial}{\partial y} + \mathbf{C} \frac{\partial^2}{\partial y^2}.$$
 (4.9b)

The individual operators become

$$\mathbf{A} = \begin{pmatrix} i\alpha & 0 & i\beta & 0 \\ \mathcal{Z} & U_y & 0 & i\alpha \\ 0 & \mathcal{Z} & 0 & 0 \\ 0 & W_y & \mathcal{Z} & i\beta \end{pmatrix}, \quad \mathbf{B} = \begin{pmatrix} 0 & 1 & 0 & 0 \\ 0 & 0 & 0 & 0 \\ 0 & 0 & 0 & 1 \\ 0 & 0 & 0 & 0 \end{pmatrix}$$
$$\mathbf{C} = \begin{pmatrix} 0 & 0 & 0 & 0 \\ -Re^{-1} & 0 & 0 & 0 \\ 0 & -Re^{-1} & 0 & 0 \\ 0 & 0 & -Re^{-1} & 0 \end{pmatrix}. \tag{4.10}$$

with $\mathcal{Z}=-i\omega+i\alpha U+i\beta W+Re^{-1}(\alpha^2+\beta^2)$. Together with boundary conditions (4.7) the system of equations (4.9) represents either a temporal or a spatial eigenvalue problem. A temporal eigenvalue problem is obtained if both α and β are prescribed as real numbers. Then ω will represent a complex-valued eigenvalue whose real part specifies the angular frequency and whose imaginary part represents the temporal growth of the corresponding eigenmode. On the other hand, a spatial eigenvalue problem is obtained if ω and β are prescribed as real-valued numbers. Then the real part of the eigenvalue α denotes the chordwise wavenumber while the imaginary part specifies the spatial growth in the chordwise direction. In general, the wavenumber α , β and the angular frequency ω are related through a dispersion relation

$$D(\alpha, \beta, \omega) = 0 \tag{4.11}$$

which is obtained by solving (4.9). Explicit forms of (4.11) are only available for some special cases.

In the following only the spatial problem is considered. Hence, the task is to compute the spatial eigenvalues α of the system (4.9) for some given ω and β . However, this is a nonlinear eigenvalue problem since α appears up to the second power in equations (4.9). In order to obtain a generalised linear eigenvalue problem (4.9) is recast into

$$i\alpha\mathcal{M}\Phi = \mathcal{N}\Phi,$$
 (4.12)

where $\Phi = (u, v, w, p, i\alpha u, i\alpha v, i\alpha w)^T$ and

$$\mathcal{N} = \begin{pmatrix}
0 & \partial/\partial y & i\beta & 0 & 0 & 0 & 0 \\
\mathcal{Z} & U_y & 0 & 0 & 0 & 0 & 0 \\
0 & \mathcal{Z} & 0 & \partial/\partial y & 0 & 0 & 0 \\
0 & W_y & \mathcal{Z} & i\beta & 0 & 0 & 0 \\
0 & 0 & 0 & 0 & 1 & 0 & 0 \\
0 & 0 & 0 & 0 & 0 & 1 & 0 \\
0 & 0 & 0 & 0 & 0 & 0 & 1
\end{pmatrix},$$
(4.13b)

with $\mathcal{Z} = -i\omega + i\beta W + Re^{-1}(\beta^2 - \partial^2/\partial y^2)$. The solution of (4.12), which - under the assumption of locally parallel flow - may be obtained for each position xseparately, provides a spectrum of spatial eigenvalues α together with the corresponding eigenmodes Φ . A numerical solution for the FSC boundary layer presented in §3 is presented in figure 4.1 for $\beta = 0.19$ and $\omega = 0$. The solution was obtained with MATLAB employing Chebyshev discretisation routines provided by Weideman & Reddy (2000). Two discrete eigenvalues as well as the discrete representation of three continuous spectrum branches become apparent. In what follows the discrete spectrum is discussed first. In section 4.1.2 some aspects of the continuous spectrum are studied.

4.1.1. The discrete spectrum - Crossflow mode

Two discrete eigenmodes become apparent in figure 4.1. The least stable one represents a crossflow disturbance while the second one is a Squire mode. Squire modes have zero wall-normal velocity components, i.e. they represent disturbances of vertical vorticity. The eigenfunction of the crossflow mode is shown in figure 4.2. The subscript 's' denotes velocities projected into the local direction of the external stream line, i.e. u_s is the velocity component in the streamline direction while v remains the wall-normal component. Figure 4.2 reveals the characteristic vortical structure of the crossflow mode. Note that, although counter-rotating, the vortices appear to be co-rotating if the meanflow is superposed. However, the streamwise velocity component u_s is clearly dominant

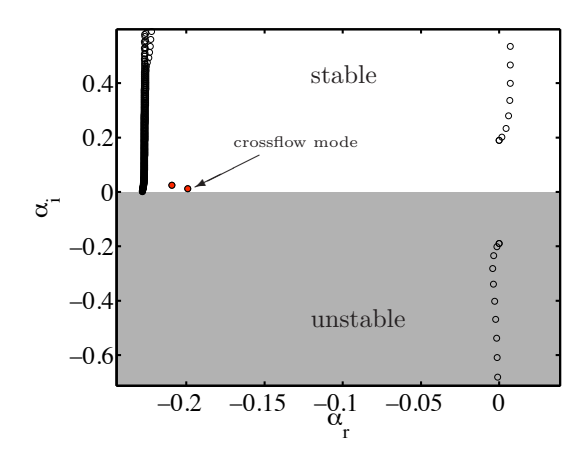


FIGURE 4.1. Spectrum of the spatial eigenvalues α in the FSC boundary layer at x=67 for $\beta=0.19$ and $\omega=0$. The shaded region denotes the unstable region. Black circles denote the numerical solution of the discretised eigenvalue problem (4.12). The red filled circles represent eigenvalues of the discrete spectrum.

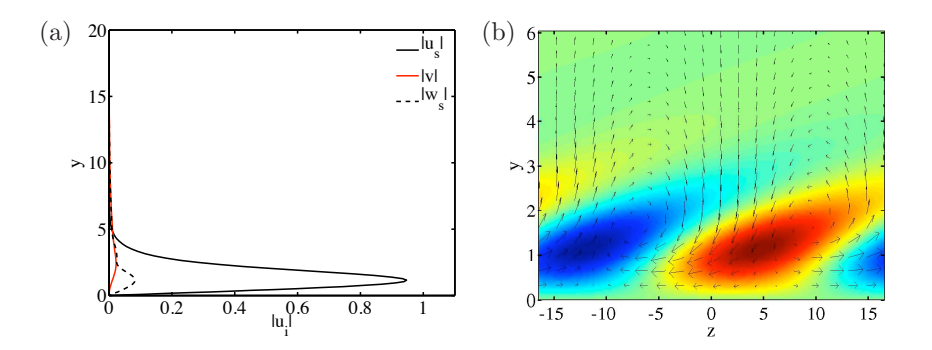


FIGURE 4.2. Crossflow mode eigenfunctions for the FSC boundary layer at x=67 with $\beta=0.19,\ \omega=0$ and $\alpha=-0.2+0.012i$. (a) Absolute values of the velocity components. (b) Pseudocolors of u_s . Vectors denote (v_s,w) .

indicating a streaky structure aligned with the external inviscid flow. If the local stability analysis presented in figure 4.2 is repeated for positions x farther downstream it is possible to follow the evolution of the crossflow mode. Figure 4.3(a) presents the local directions of the respective line of constant phase, *i.e.* $\phi = -\arctan(\alpha/\beta)$, as well as the external streamline where $\phi = \arctan W/U$.

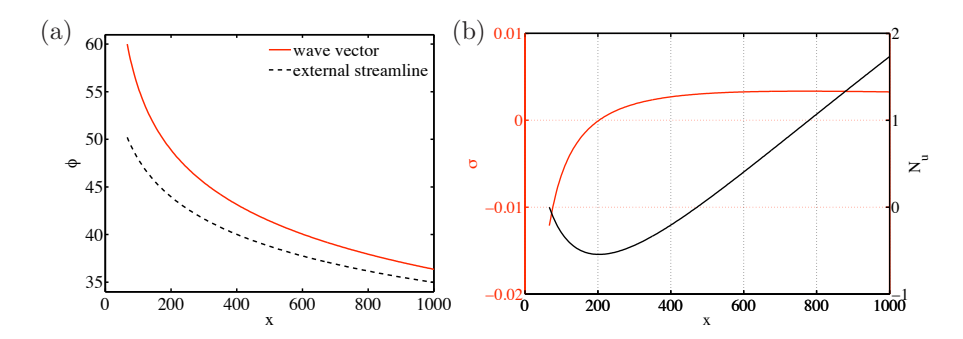


FIGURE 4.3. Spatial evolution of the crossflow mode detected in figure 4.1. (a) Local angle of both the line of constant phase and the external streamline with respect to the x-direction. (b) Growth rate $\sigma = -\alpha_i$ and N-factor $N_u = \ln(|u/u(x_n)|)$.

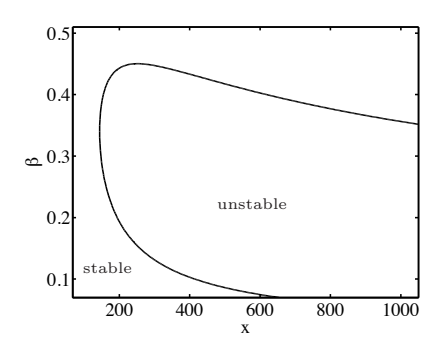


FIGURE 4.4. Neutral curve of the FSC boundary layer for steady crossflow disturbances with $\beta \in [0.07, 0.5]$.

Here, ϕ defines the local angle between the direction of either the line of constant phase or the external streamline and the x-direction. It is apparent that the line of constant phase predicted by local theory does not exactly coincide with the external streamline. They are close though, explaining the experimental observations previously mentioned.

At some position x the eigenvalue which is related to the crossflow mode will have $\alpha_i=0$ and the disturbance will thus be neutrally stable. Moving even farther downstream it will flip into the unstable region; the crossflow mode grows. The spatial growth of the crossflow mode is depicted in figure 4.3(b). The neutral point of the steady crossflow mode studied here is located at x=200. Downstream of the neutral point the crossflow mode grows and reaches an N-Factor of almost 2 at x=1000. If the growth rates σ of various steady crossflow modes with $\beta \in [0.07, 0.5]$ are computed it is possible to draw the neutral curve in figure 4.4 by considering the contour of zero growth. Hence,

based on local theory, the first stationary mode that becomes unstable has $\beta = 0.35$. For x < 146 and $\beta > 0.45$ stationary crossflow disturbances are stable and thus decay exponentially.

4.1.2. The continuous spectrum

The spatial domain of a boundary layer flow is semi-infinite. A Fourier representation of a solution to the governing differential equations thus requires a continuous set of modes (cf. Schmid & Henningson 2001), i.e. the continuous spectrum modes. Initially, the continuous spectrum of the local stability problem was studied by Grosch & Salwen (1978). Further comprehensive information on the continuous spectrum and how it may be used to represent general solutions may be found in Ashpis & Reshotko (1990); Schmid & Henningson (2001) and various publications by Tumin & coworkers (see e.g. Tumin 2003). The discrete representation of the continuous spectrum shown in figure 4.1 was obtained numerically for a finite number of modes. It therefore depends on the numerical method as well as the domain size and resolution chosen. However, it is possible to give an explicit expression for the eigenvalues of the continuous spectrum. These are derived in the following by considering asymptotic solutions at $y \to \infty$ (see also Mack 1984, who provides similar asymptotic solutions for three-dimensional boundary layers).

For $y \to \infty$ the baseflow derivatives with respect to y vanish and the operator \mathcal{L}_l consists of constant coefficients only. Explicit solutions in the free-stream are obtained by recasting the equation system (4.9) into

$$\frac{\partial \psi}{\partial y} = \mathcal{H}\psi \tag{4.14}$$

with $\psi = (u, v, w, p, u_v, w_v)^T$. At $y \to \infty$, \mathcal{H} becomes

$$\mathcal{H} = \begin{pmatrix} 0 & 0 & 0 & 0 & 1 & 0 \\ -i\alpha & 0 & -i\beta & 0 & 0 & 0 \\ 0 & 0 & 0 & 0 & 0 & 1 \\ 0 & -\mathcal{Z} & 0 & 0 & -Re^{-1}i\alpha & Re^{-1}i\beta \\ Re \mathcal{Z} & 0 & 0 & Re i\alpha & 0 & 0 \\ 0 & 0 & Re \mathcal{Z} & Re i\beta & 0 & 0 \end{pmatrix}$$
(4.15)

with $\mathcal{Z} = -i\omega + i\beta W + i\alpha U + Re^{-1}(\alpha^2 + \beta^2)$. In the free-stream, the solutions of (4.14) will then take the form

$$\psi_j(y) = \Psi_j e^{\lambda_j y},\tag{4.16}$$

where λ_i denotes the characteristic value of the j^{th} fundamental solution Ψ_i . The six characteristic values are readily obtained as

$$\lambda_{1,2} = \pm \sqrt{\alpha^2 + \beta^2}$$
(4.17a)
$$\lambda_{3,4} = \pm \sqrt{Re(-i\omega + i\beta W + i\alpha U) + \alpha^2 + \beta^2}$$
(4.17b)
$$\lambda_{5,6} = \lambda_{3,4}$$
(4.17c)

$$\lambda_{3.4} = \pm \sqrt{Re(-i\omega + i\beta W + i\alpha U) + \alpha^2 + \beta^2}$$
 (4.17b)

$$\lambda_{5,6} = \lambda_{3,4} \tag{4.17c}$$

together with the fundamental solutions

$$\Psi_{1,2} = \begin{pmatrix} \alpha \\ -i\lambda_{1,2} \\ \beta \\ \omega - \alpha U - \beta W \\ \alpha\lambda_{1,2} \\ \beta\lambda_{1,2} \end{pmatrix}, \Psi_{3,4} = \begin{pmatrix} 1 \\ -\frac{i\alpha}{\lambda_{3,4}} \\ 0 \\ 0 \\ \lambda_{3,4} \\ 0 \end{pmatrix}, \Psi_{5,6} = \begin{pmatrix} 0 \\ -\frac{i\beta}{\lambda_{5,6}} \\ 1 \\ 0 \\ 0 \\ \lambda_{5,6} \end{pmatrix}.$$
(4.18)

Here, λ_1 , λ_3 and λ_5 are chosen to have negative real parts. By inspection of these fundamental solutions one may classify continuous spectrum modes as vortical and pressure waves. Computing the vorticity components of $\Psi'_{1,2} = \Psi_{1,2}e^{i\alpha x + i\beta z - i\omega t}$, e.g. the wall-normal vorticity component

$$\frac{\partial v'}{\partial x} - \frac{\partial u'}{\partial y} = (\alpha \lambda_{1,2} - (-i\lambda_{1,2})i\alpha) e^{i\alpha x + i\beta z - i\omega t} = 0, \tag{4.19}$$

it is clear that the continuous spectrum modes associated with $\lambda_{1,2}$ do not exhibit vorticity and are thus classified as pressure modes. The other four fundamental solutions Ψ_{3-6} do not comprise a pressure component but have non-zero vorticity and are thus referred to as vorticity modes.

As opposed to modes belonging to the discrete spectrum, continuous spectrum modes are not required to decay in the free-stream but to be bounded. Hence, in order to obtain eigenvalues of the continuous spectrum branches associated with the pressure modes, α is computed from (4.17a) with $\lambda_{1,2}=\pm i\gamma$. Here, γ can be seen as a wall-normal wavenumber. Accordingly, $\lambda_{3,4}=\lambda_{5,6}=\pm i\gamma$ are chosen in (4.17b), (4.17c) to obtain eigenvalues α corresponding to the vorticity mode branch. This results in four continuous spectrum branches. Three of them, one vorticity mode branch and two pressure mode branches, are shown in figure 4.5 together with the discrete representation presented earlier. Those continuous modes having $\Im(\alpha)<0$, *i.e.* one pressure mode branch and the second vorticity branch not shown in figure 4.1, describe the flow response upstream of any disturbance source (cf. Ashpis & Reshotko 1990). Those modes located in the upper half plane of figure 4.5 are associated with the downstream response of the flow.

Downstream vortical modes of the continuous spectrum will be used later to model receptivity to free-stream disturbances. In the free-stream, the associated full eigenfunctions are a linear combination of four fundamental solutions (4.18). In the case of vortical modes there exist two linear independent solutions which are referred to as 'Mode A' and 'Mode B'. Their respective definition is given by Tumin (2003) as

$$\psi_A = a_A \Psi_1 + b_A \Psi_3 + c_A \Psi_4 + d_A \Psi_5 \tag{4.20}$$

$$\psi_B = a_B \Psi_1 + b_B \Psi_4 + c_B \Psi_5 + d_B \Psi_6, \tag{4.21}$$

where the respective coefficients a, b, c and d can be determined numerically based on no-slip boundary conditions at the wall, *i.e.* u = v = w = 0, and

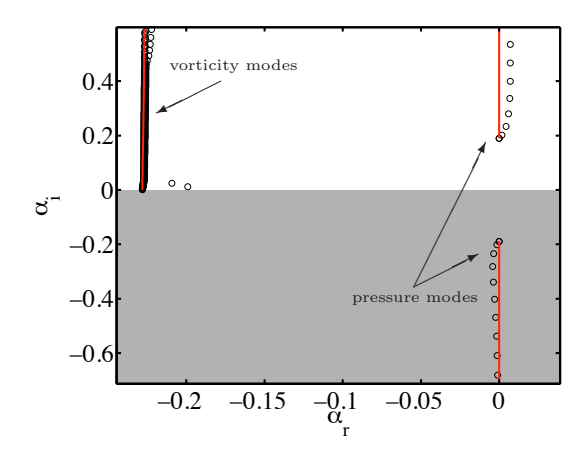


FIGURE 4.5. Spectrum of the spatial eigenvalues α in the FSC boundary layer at x=67 for $\beta=0.19$ and $\omega=0$. The shaded region denotes the unstable region. Black circles denote the numerical solution of the discretised eigenvalue problem (4.12) whereas the asymptotic solution of the continuous spectrum is represented by the red lines.

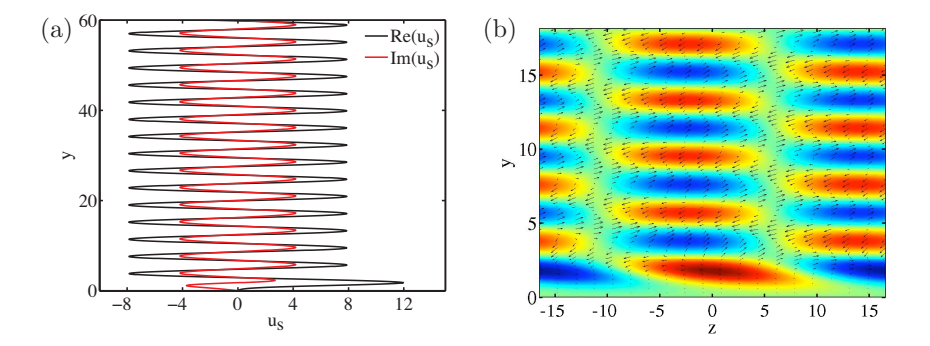


FIGURE 4.6. Vorticity mode (Mode A) associated with the continuous spectrum of the FSC boundary layer at x=67 for $\beta=0.19,\,\omega=0,\,\gamma=-1$ and $\alpha=0.377+0.016i$. (a) Real and imaginary part of the velocity component u_s . (b) Pseudocolors of u_s . Vectors denote (v_s,w) .

one normalisation condition, e.g. $\partial u/\partial y = 1$ at the wall. An example of one continuous vorticity mode (Mode A) in the FSC boundary layer is shown in figure 4.6. One can clearly see the oscillatory behaviour of the mode outside the boundary layer. The vectors in figure 4.6 nicely visualise the vortical

behaviour of these modes in the free-stream.

In this work continuous modes were solely used as inflow conditions in order to study the receptivity to free-stream disturbances. However, they form a complete basis for general solutions of the local stability problem. As such they may be used to compute spatial optimal disturbances (cf. Tumin & Reshotko 2001) or to decompose flow fields obtained from numerical simulations or experiments (cf. Tumin 2003).

4.2. Nonlocal stability theory

The assumption of a locally parallel baseflow allows to efficiently study the physical instability mechanisms of boundary layers. However, especially in crossflow-dominated boundary layers, the spatial evolution of disturbances is significantly affected by baseflow nonparallelism. Several simplifications of the full stability equations (4.5) accounting for nonparallelism have been developed. The parabolised stability equations (PSE) have been the basis of several papers presented in this thesis and are introduced in this section.

For convectively unstable flows a spatial nonlocal stability theory commonly known as the parabolised stability equations was independently developed by Herbert & Bertolotti (Bertolotti 1991; Bertolotti et al. 1992; Herbert 1997) and by Simen & Dallmann (Simen 1992). The fundamental idea behind the PSE is to decompose the disturbance into a slowly varying and a fast oscillatory part. Accordingly the following modal ansatz is made where the disturbance \mathbf{q}' is decomposed into a shape function \mathbf{q} and a phase function Θ according to

$$\mathbf{q}'(x,y,z,t) = \mathbf{q}(x,y)\Theta(x)e^{i\beta z - i\omega t} + c.c.$$

$$\Theta(x) = e^{i\int_{x_0}^x \alpha(x')dx'},$$
(4.22a)

$$\Theta(x) = e^{i\int_{x_0}^x \alpha(x')dx'}, \tag{4.22b}$$

where $\mathbf{q} = (u, v, w, p)^T$ and $\hat{\mathbf{q}} = \mathbf{q}\Theta$. In (4.22a) the shape function is assumed to be slowly varying in the chordwise direction x while the exponential part is assumed to capture the disturbance oscillations. However, the solution ansatz (4.22a) causes an ambiguity since both the shape function \mathbf{q} and the chordwise phase function Θ are functions of the chordwise coordinate x. This ambiguity is resolved by choosing α such that the assumption of a slowly varying shape function is valid. Two different approaches are chosen in the following depending on the type of disturbance studied. A classical approach is used to study the evolution of modal disturbances while a modified approach is employed to compute the evolution of more general disturbances. Both approaches are explained in section 4.2.2.

Further, a scale separation between variations in chordwise and wall-normal direction is introduced. It is assumed that variations in chordwise direction are much slower than variations in wall-normal direction. Hence, after introducing (4.22a) into (4.5) chordwise derivatives and the wall-normal mean velocity

component are assumed to be of order $\mathcal{O}(Re^{-1})$, i.e.

$$\frac{\partial}{\partial x}, V \to \mathcal{O}(Re^{-1}).$$
 (4.23)

Identifying and neglecting all terms which are of order $\mathcal{O}(Re^{-2})$ and higher leads to a quasi-parabolic equation system of the form

$$\mathcal{L}_{p}\mathbf{q} = 0 \tag{4.24}$$

with \mathcal{L}_p being the linear operator

$$\mathcal{L}_p = \mathbf{A} + \mathbf{B} \frac{\partial}{\partial y} + \mathbf{C} \frac{\partial^2}{\partial y^2} + \mathbf{D} \frac{\partial}{\partial x}.$$
 (4.25)

For a simple non-curved geometry the operators A, B, C and D become

$$\mathbf{A} = \begin{pmatrix} i\alpha & 0 & i\beta & 0 \\ U_x + \mathcal{Z} & U_y & 0 & i\alpha \\ 0 & V_y + \mathcal{Z} & 0 & 0 \\ W_x & W_y & \mathcal{Z} & i\beta \end{pmatrix}, \qquad \mathbf{B} = \begin{pmatrix} 0 & 1 & 0 & 0 \\ V & 0 & 0 & 0 \\ 0 & V & 0 & 1 \\ 0 & 0 & V & 0 \end{pmatrix}$$
(4.26a)
$$\mathbf{C} = \begin{pmatrix} 0 & 0 & 0 & 0 & 0 \\ -Re^{-1} & 0 & 0 & 0 & 0 \\ 0 & -Re^{-1} & 0 & 0 & 0 \\ 0 & 0 & -Re^{-1} & 0 \end{pmatrix}, \quad \mathbf{D} = \begin{pmatrix} 1 & 0 & 0 & 0 \\ U & 0 & 0 & (1) \\ 0 & U & 0 & 0 \\ 0 & 0 & U & 0 \end{pmatrix},$$
(4.26b)

where

$$\mathcal{Z} = -i\omega + i\alpha U + i\beta W + \frac{1}{Re}(\alpha^2 + \beta^2). \tag{4.27}$$

Introducing an initial disturbance \mathbf{q}_0 at a chordwise position x_0 the PSE (4.24) can be solved by simply marching downstream while solutions subject to boundary conditions

$$u = v = w = 0$$
 at $z = 0$, (4.28a)

$$u \to 0, v \to 0, w \to 0$$
 as $z \to \infty$ (4.28b)

are required. The system (4.24) is only quasi-parabolic in that it exhibits an inherent ellipticity which can cause numerical instabilities at small stepsizes Δx (see e.g. Li & Malik 1996, 1997; Andersson et al. 1998). In order to relax this numerical instability the disturbance pressure gradient p_x (term (1) in 4.26b) is omitted in the chordwise momentum equation as was proposed by Haj-Hariri (1994). By comparing to DNS results, it is shown in papers 1 & 2 that, in the case of crossflow-dominated boundary layers, this term has only negligible effects on the computed results.

4.2.2. Closure & Choice of
$$\alpha$$

As discussed previously, the disturbance ansatz (4.22) does not imply a unique definition of a chordwise wavenumber α . A choice has to be made for α such that the shape function \mathbf{q} may be assumed to be slowly varying. Within the framework of local stability theory the wavenumber α is well defined. Based

on the local ansatz (4.8), it could be retained from the solution \mathbf{q}' as the logarithmic derivative

$$\alpha = -i\frac{\partial(\ln \mathbf{q}')}{\partial x} = -i\frac{1}{\mathbf{q}'}\frac{\partial \mathbf{q}'}{\partial x},\tag{4.29}$$

while α is independent of the wall-normal position or the disturbance quantity chosen. Following Bertolotti *et al.* (1992) and Hanifi *et al.* (1994) a physical complex wavenumber $\tilde{\alpha}$ may be defined similarly in the nonlocal framework based on (4.22) as

$$\tilde{\alpha}(x,y) = -i\frac{\partial(\ln \mathbf{q}')}{\partial x} = \alpha(x) - i\frac{1}{\mathbf{q}}\frac{\partial \mathbf{q}}{\partial x}.$$
(4.30)

However, (4.30) is a vector function of the wall-normal position. According to Herbert (1994) a scalar quantity independent of y is obtained if (4.30) is multiplied with $\mathbf{q}^H \mathbf{q}$, integrated over y and divided by the integral of $\mathbf{q}^H \mathbf{q}$ yielding

$$\frac{\int_0^\infty \tilde{\alpha} \, \mathbf{q}^H \mathbf{q} \, \mathrm{d}y}{\int_0^\infty \mathbf{q}^H \mathbf{q} \, \mathrm{d}y} = \alpha(x) - i \frac{\int_0^\infty \mathbf{q}^H (\partial \mathbf{q}/\partial x) \, \mathrm{d}y}{\int_0^\infty \mathbf{q}^H \mathbf{q} \, \mathrm{d}y}.$$
 (4.31)

On the basis of (4.31) a classical choice, ensuring minimal streamwise changes of \mathbf{q} across y, is represented by the Norm

$$\int_{0}^{\infty} \mathbf{q}^{H} \frac{\partial \mathbf{q}}{\partial x} \, \mathrm{d}y = 0. \tag{4.32}$$

Hence, if **q** satisfies the Norm (4.32) both the growth and the periodic oscillations of \mathbf{q}' are captured by the phase function (4.22b) while both $\partial \mathbf{q}/\partial x$ and $\partial \alpha/\partial x$ remain small.

The PSE equations (4.25) together with norm (4.32) build a coupled nonlinear system which, on the basis of the preceding upstream solutions, can be solved locally at each chordwise position x employing iterative techniques such as Newton's or related methods. The required initial guess is provided by the solution obtained for the respective previous position. Initially, the latter is represented by the solution of the local stability problem.

However, if no initial guess for the complex chordwise wavenumber is known, which is the case for more general, non-modal disturbances, a different approach has been chosen here. Again, the aim is to choose α such that the variation of \mathbf{q} in the streamwise direction is small. In order to fulfil this requirement it is considered sufficient in the following to remove only periodic oscillations from the shape function \mathbf{q} . Hence, α is chosen as a real number and the growth of \mathbf{q}' will be absorbed by \mathbf{q} . Starting again from the definition of a nonlocal physical wavenumber (4.30), a well-defined, real- and scalar-valued wavenumber α is obtained by the choice

$$\tilde{\alpha} = \alpha - \Re\left(i\frac{1}{A}\frac{\partial A}{\partial x}\right). \tag{4.33}$$

 \Re and \Im represent real and imaginary parts of a complex number respectively and A(x) represents a complex amplitude such that $\mathbf{q}(x,y) = A(x)\tilde{\mathbf{q}}(x,y)$. Here, $\tilde{\mathbf{q}}$ denotes the normalised disturbance quantities. There is no unique choice for A(x). However, it makes sense to consider the dominant disturbance velocity component. In a crossflow dominated boundary layer the latter is usually represented by u_{cp} which is the disturbance velocity component tangential to the line of constant phase of the disturbance wave of interest. Hence, in the following A is chosen as

$$A(x) = u_{cp}(x, y_{max}), \tag{4.34}$$

where y_{max} denotes the wall-normal position at which $|u_{cp}|$ reaches its maximum. Requiring all periodic oscillations of \mathbf{q}' to be captured by the exponential part of (4.22) implies

$$\Re(-i\frac{1}{A}\frac{\partial A}{\partial x}) = 0. \tag{4.35}$$

In practice, the latter condition can be satisfied approximately by determining α iteratively on the basis of (4.33). As an initial guess α is obtained based on the observation that crossflow and non-modal disturbances are closely aligned with the outer streamline in crossflow-dominated boundary layers (cf. §4.1.1). In the next iteration step $\alpha = \tilde{\alpha}$ is chosen. The latter step is repeated until the energy growth has converged.

Compared to the first, classical approach described above this approach is more robust with respect to the initial guess of α . The normalisation (4.35) is only enforced approximately in a global sense as opposed to the more restrictive norm (4.32) which is enforced locally. A good robustness is needed to be able to compute the spatial evolution of general non-modal disturbances for which a wavenumber based on the external streamline is just a rough first estimate, yet the best available. Further, the choice of a real-valued wavenumber does not require an initial guess for the growth of the disturbance. While it is certainly possible to also capture the growth of \mathbf{q}' in the phase function Θ , *i.e.* choosing $\tilde{\alpha}$ to be complex-valued with an imaginary part

$$\Im(\tilde{\alpha}) = \Im\left(\alpha - i\frac{1}{A}\frac{\partial A}{\partial x}\right) \tag{4.36}$$

on the basis of previous iterations, such a choice was found to degrade the convergence characteristics for general, non-modal disturbances.

Applications of this second approach for closure can be found in $\S5.2.3$ and $\S6$ as well as in papers 1 & 2. Note that the methods employed in paper 1 and by Tempelmann *et al.* (2010) are identical but described from a different viewpoint.

4.2.3. Nonlinear PSE

A nonlinear extension of the PSE exists and shall be briefly introduced here. It allows for predicting the nonlinear evolution of modal instabilities. It is

obtained by introducing the disturbance ansatz

$$\mathbf{q}'(x, y, z, t) = \sum_{m} \sum_{n} \mathbf{q}_{mn}(x, y) \exp\left[i \int_{x_0}^{x} \alpha_{mn}(x') \, \mathrm{d}x' + in\beta z - im\omega t\right]$$
(4.37)

into the nonlinear equivalent of equation (4.3), *i.e.* the nonlinear disturbance equations. The subscripts m and n denote modal disturbances with $(m\omega, n\beta)$. This leads to a coupled nonlinear system of quasi-parabolic equations of the form

$$\mathcal{L}_{mn}\mathbf{q}_{mn} = \mathbf{f}_{mn} \tag{4.38}$$

for the Fourier component \mathbf{q}_{mn} . The operator \mathcal{L}_{mn} is identical to its linear counterpart \mathcal{L}_p but depends nonlinearly on α_{mn} . The forcing term \mathbf{f}_{mn} represents the Fourier transform of the nonlinear terms. Numerically, the nonlinear PSE are solved by marching downstream starting with a solution to the local stability problem for a certain number of modes. At each position x the nonlinear system of equations (4.38) together with a normalisation for each mode, e.g. (4.32), is solved iteratively, where new harmonics are introduced when forced by the right-hand side of (4.38). More information about the nonlinear PSE can be found in Bertolotti et al. (1992), Hein et al. (2000) and Schmid & Henningson (2001).

4.2.4. PSE results for the FSC boundary layer

A few results obtained by employing the linear PSE to the FSC boundary layer introduced in §3 are presented in this section. To highlight nonparallel effects the PSE solutions are compared with those of the local stability analysis presented in the previous section. Further, results are compared with DNS solutions of the LNSE (4.5) in order to evaluate the validity of assumptions accompanying the PSE.

The spatial evolution of a disturbance as predicted by nonlocal theory is commonly presented in the form of growth rates and N-factors. These are defined as

$$\sigma_u = -\Im(\tilde{\alpha}) \tag{4.39}$$

$$N_u = \ln\left(\frac{A}{A_0}\right),\tag{4.40}$$

where the subscript 'u' denotes a disturbance amplitude A which represents the wall-normal maximum of the chordwise disturbance velocity component. PSE results obtained for the steady crossflow are presented in figure 4.7 and compared to solutions of the LNSE as well as to the local stability results presented in the previous section. The spatial evolution predicted by solving the PSE is in excellent agreement with the DNS results. The comparison presented in figure 4.7 thus provides an impressive validation of the PSE method. Further it is shown that, in terms of quantitative predictions, results obtained from local theory are not satisfactory. While the growth predicted based on local theory gets close to DNS and PSE results towards the end of the domain a significant

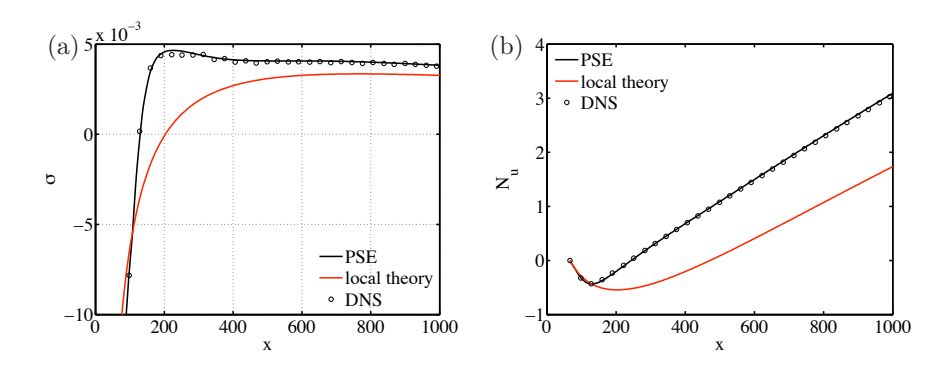


FIGURE 4.7. Spatial evolution of a crossflow mode with $\beta = 0.19$ and $\omega = 0$. Growth rate σ_u (a) and the corresponding N-factor N_u (b) as predicted by PSE, DNS and local theory.

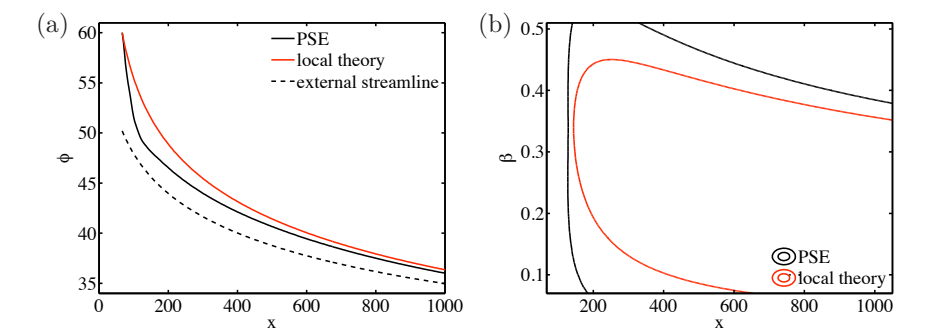


FIGURE 4.8. Comparison of PSE solutions with those obtained from local theory. (a) Local angle of the line of constant phase for a crossflow mode with $\beta=0.19$ and $\omega=0.0$ compared with the angle of the external streamline. (b) Neutral curve of the FSC boundary layer for steady crossflow modes with $\beta \in [0.07, 0.5]$.

discrepancy is observed in the vicinity of the neutral point, *i.e.* where $\sigma_u = 0$. However, it is exactly this region where disturbances are known to be most sensitive to *e.g.* inhomogeneous boundary conditions (*cf.* Crouch 1993; Pralits *et al.* 2000) and which is thus important for receptivity analyses. A similar trend is found when comparing the wavevectors resulting from the PSE as well as the local solution (see figure 4.8 a). These are principally similar. However, a significant discrepancy is apparent in the region of the neutral point. While the line of constant phase predicted by PSE follows the external streamline more closely than that predicted by local theory it is still not perfectly aligned. The neutral curve obtained by solving the PSE for different steady crossflow modes is shown in figure 4.8. Again, local theory is found to yield similar results

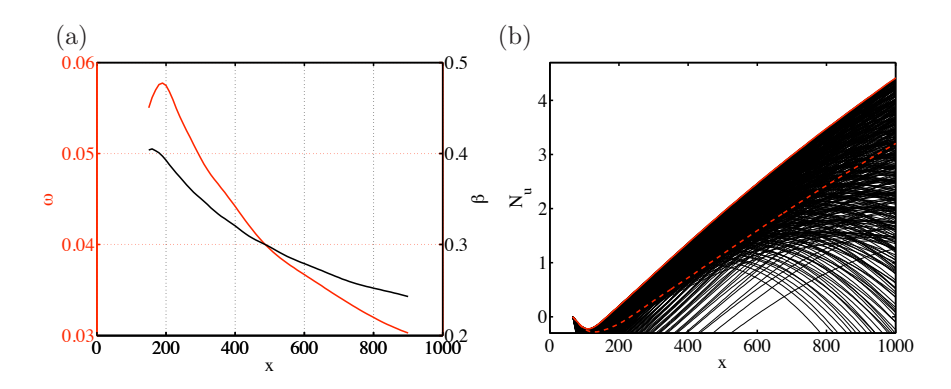


FIGURE 4.9. PSE solutions of crossflow modes in a FSC boundary layer with $\omega \in [0.0, 0.1]$ and $\beta \in [0.07, 0.5]$. (a) Frequency and wavenumber corresponding to the most dominant mode at each position x. (b) N-factors of all considered modes. The red line represents the envelope providing the N-factor of the dominant mode at each position x. The red dashed line denotes the respective envelope of the stationary disturbances.

in a qualitative sense as the trend of both neutral curves shown is similar. However, the chordwise locations of branch 1 and branch 2 are significantly different especially for the lower and higher spanwise wavenumbers considered. Note, that the neutral curve predicted by nonlocal theories will depend on the position of initialisation. If the modes would have been initiated farther upstream, the neutral curve would also have shifted slightly upstream. For more details the reader is referred to paper 1.

So far, only steady disturbances have been considered. These are not the most unstable ones though as can be seen in figure 4.9 where the PSE have been solved for both stationary and non-stationary crossflow modes. All modes were initialised at the same position $x_0 = 67$. It is apparent from figure 4.9 (a) that the dominant scales inside the boundary layer become larger. Both the frequency and the spanwise wavenumber of the dominant mode decrease with x. The maximum N-factor that can be obtained at each position x when both stationary and non-stationary modes are accounted for is larger than that obtained for stationary modes only. Hence, if both types of modes would be initiated with similar amplitudes, non-stationary disturbances would dominate the boundary layer. However, the receptivity mechanisms of steady and unsteady disturbances are different. It is not possible to predict the dominant disturbances inside a boundary layer without a comprehensive and quantitative receptivity analysis. The latter will be the topic of the following sections.

Once an initial amplitude is known from such a receptivity study the non-linear PSE can be employed to predict the spatial evolution of crossflow modes even at higher amplitudes when nonlinear effects become important. One such

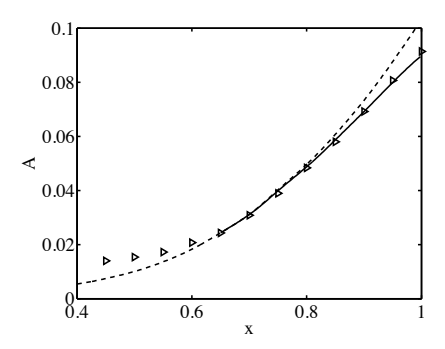


Figure 4.10. Disturbance amplitude A obtained from experiments by Kurian $et~al.~(2011)~(\diamond)$ for a FSC-like boundary layer. Linear evolution of the dominant unsteady crossflow mode as predicted by linear PSE (---) and nonlinear PSE (---). The nonlinear PSE were initialised at x=0.65 with an amplitude extracted from the experimental measurements.

example is given in figure 4.10. The disturbance amplitudes shown were measured by Kurian $et\ al.\ (2011)$ for a FSC-like swept-flat-plate boundary layer. The linear growth of a crossflow mode is found to match the experimental measurements only in a short region downstream of x=0.65. Upstream of that position the disturbance field is dominated by non-modal growth (for details the reader is referred to Tempelmann 2009). If the nonlinear PSE are initialised with an amplitude extracted from the experiments at x=0.65 the predicted evolution farther downstream perfectly matches the experimental measurements. The final aim of a receptivity analysis is to provide the initial modal amplitude solely based on knowledge about the external disturbance environment which in this case was free-stream turbulence.

CHAPTER 5

Receptivity

As demonstrated in the previous section, it is important to determine initial amplitudes of boundary-layer disturbances in order to identify dominant modes. These initial amplitudes are governed by the external disturbance environment, e.g. by free-stream turbulence, surface roughness or acoustic noise. The aim of any receptivity analysis therefore is to provide initial disturbance amplitudes inside the boundary layer on the basis of a specific external disturbances environment. The methods for receptivity prediction presented in the following may be classified into direct and indirect methods.

5.1. Direct receptivity computations

Here, it shall be referred to direct receptivity methods if the external disturbance environment is directly accounted for when solving the LNSE or PSE. For example, receptivity to surface roughness may be studied by inserting the roughness elements into the computational grid. Receptivity to free-stream turbulence, on the other hand, could be studied by triggering turbulence in the free-stream.

5.1.1. Receptivity to surface roughness

In the following the receptivity to surface roughness is studied by solving the LNSE. The roughness is not inserted into the computational grid but modelled as inhomogeneous wall-boundary conditions. This can be accomplished by projecting the no-slip conditions on the surface of the roughness to the undisturbed wall using Taylor-series expansions. Accordingly the inhomogeneous boundary conditions for a disturbance of spanwise wavenumber β become

$$\hat{u}(x, y = 0) = -H_{\beta}(x) \frac{\partial U}{\partial y}$$
 (5.1a)

$$\hat{v}(x, y = 0) = 0 \tag{5.1b}$$

$$\hat{u}(x, y = 0) = -H_{\beta}(x) \frac{\partial U}{\partial y}$$

$$\hat{v}(x, y = 0) = 0$$

$$\hat{w}(x, y = 0) = -H_{\beta}(x) \frac{\partial W}{\partial y}$$

$$(5.1a)$$

$$(5.1b)$$

where the roughness shape h(x,z) is represented by discrete Fourier modes $H_{\beta}(x)$. These boundary conditions can be easily imposed at the wall in direct numerical simulations of the LNSE and there is no need to modify the computational grid. In paper 3 it is shown that the performance of this roughness model is excellent up to roughness heights of about 10% of the displacement thickness. For larger roughness heights, receptivity becomes nonlinear.

While it is certainly possible to allow for inhomogeneous boundary conditions in the PSE it is not straightforward to quantitatively predict the receptivity to boundary conditions of the type (5.1). This is because the latter will excite many different modes leading to a strong transient and thus inherently nonparallel behaviour of the disturbance which may not be captured correctly by the PSE. Nonetheless, Herbert (1993) studied the excitation of crossflow vortices to wall blowing/suction and obtained results which were in qualitative agreement to experiments with surface roughness. An idea on how to resolve the mentioned problem was given by Bertolotti (2000). He suggested to apply a bandpass filter to the wall forcing (5.1) centred at the wavenumber α of the eigenmode of interest. Such a filter would remove energy from those modes decaying in the farfield and thus all the initial transient effects that would require highly resolved DNSs. However, in this thesis well-resolved direct LNSE computations have been performed to study receptivity to surface roughness.

The shape of surface roughness considered for the FSC boundary layer is chosen according to Schrader *et al.* (2009). It is defined as

$$h(x,z) = \varepsilon_h H_\beta(x) \sin(\beta_R z), \tag{5.2}$$

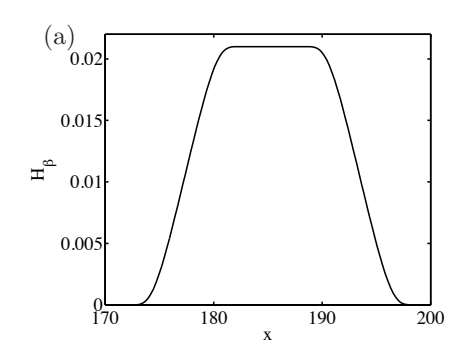
where ε_h denotes the height of the roughness, $\beta_R = 2\pi/L_z$ the spanwise wavenumber and L_z the width of the computational domain. The chordwise shape H_β is provided by

$$H_{\beta}(x) = \left[S\left(\frac{x - h_s}{h_r}\right) - S\left(\frac{x - h_e}{h_f} + 1\right) \right],\tag{5.3}$$

where S is a smooth step function defined in Schrader $et\ al.\ (2009)$ and h_s, h_e define the position and the extension of the roughness element. The roughness position x_r may be defined as $h_s + (h_e - h_s)/2$. The parameters h_f, h_r affect the shape of the element and have been chosen constant for all considered roughness positions. The roughness shape chosen throughout this study is depicted in figure 5.1(a) for $x_r = 185.4$. The response of the FSC boundary layer to this roughness element as obtained from a solution of the LNSE is shown in figure 5.1(b) for two different roughness positions. A strong peak of the disturbance amplitude becomes apparent at the respective roughness position. Just downstream of the peak the disturbance evolution is characterised by exponential growth. This indicates that all excited modal disturbances except the crossflow mode decay quickly. No transient growth is observed. Receptivity to the roughness element located farther downstream is weaker. A more general discussion on the dependence of receptivity on the roughness location is given in §5.2.

$5.1.2.\ Receptivity\ to\ free-stream\ disturbances$

The receptivity of a boundary layer to free-stream disturbances can be studied prescribing inhomogeneous inflow boundary conditions. Vortical free-stream



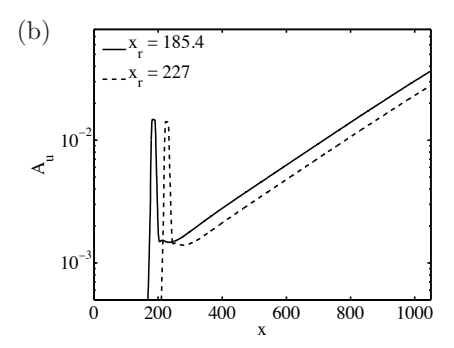


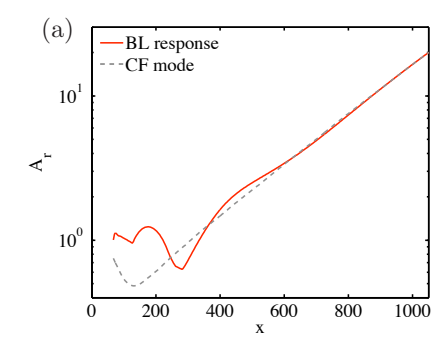
FIGURE 5.1. (a) Shape function $H_{\beta}(x)$ of the roughness element for $h_s=171.6$, $h_e=199.2$, $h_r=h_f=11.5$. Hence, the depicted roughness position is $x_r=185.4$. The height of the roughness element is chosen as $\epsilon_r=0.021$. (b) Boundary layer response to surface roughness for $\beta=0.19$ and two different roughness positions. The amplitude is defined as $A_u=\max_y |u|$.

disturbances of type 'Mode A', stemming from the continuous spectrum of the local stability operator (cf. §4.1.2), are chosen in the following. These are considered to represent an appropriate basis for modelling free-stream turbulence (cf. Jacobs & Durbin 2001; Brandt $et\ al.$ 2004). By solving the LNSE, Schrader $et\ al.$ (2009) were the first to study receptivity of three-dimensional boundary layers to this type of disturbances. Employing PSE, the receptivity to continuous spectrum modes was only computed for two-dimensional boundary layers by Lin $et\ al.$ (1995).

Figure 5.2 (a) shows the response of the FSC boundary layer to a steady vortical continuous spectrum mode. Here, the continuous mode is prescribed at $x_0 = 67$ and the disturbance evolution is computed by solving the PSE. Note that the wavenumber α is determined locally based on Norm (4.32). The boundary layer response is characterised by comparing with the PSE solution of the corresponding clean crossflow disturbance. Receptivity to free-stream disturbances is quantified by a normalised receptivity amplitude

$$A_r(x) = \frac{\max_y |u(x)|}{\max_y |u(x_0)|},$$
(5.4)

where $u(x_0)$ represents the vortical free-stream mode. Initially, the boundary layer response is characterised by non-modal behaviour until, for x > 500, the crossflow mode becomes dominant. Since free-stream turbulence involves vortical flow structures of various different scales, it makes sense to study the receptivity to vortical free-stream modes of different scales. Figure 5.2 depicts the receptivity amplitude of the boundary layer response to continuous spectrum modes with different wall-normal wave numbers γ . It is apparent that



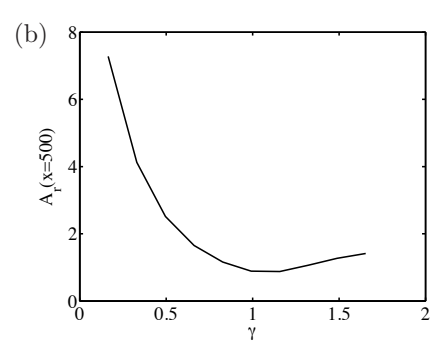


FIGURE 5.2. Receptivity to vortical free-stream disturbances as predicted by solving the direct PSE. (a) Response of the FSC boundary layer to a vortical free-stream mode (Mode A) with $\beta=0.19,\,\gamma=0.3$ and $\omega=0$. (b) Receptivity amplitudes for vortical free-stream modes with $\gamma\in[0.165,1.65]$.

strongest receptivity is obtained for vorticity modes with large wall-normal length scales. However, the receptivity amplitude does not decrease monotonically with increasing γ but increases again for $\gamma>1.2$. This observation is consistent with results by Schrader et al. (2009). By solving the LNSE, these authors performed an extensive parametric study on this receptivity mechanism. They found the efficiency of the receptivity mechanism to increase for small wall-normal length scales due to deep penetration of the corresponding continuous modes into the boundary layer.

5.2. Receptivity modelling using adjoint solutions

Adjoint solutions represent a very efficient tool for predicting receptivity. The following two citations illustrate how adjoint solutions may be used for receptivity modelling. In his article "A 'receptive' boundary layer" Bottaro (2010) writes

Receptivity is the process which describes how environmental disturbances (such as gusts, acoustic waves or wall roughness) are filtered by a boundary layer and turned into downstream-growing waves.

Hill (1995) writes in his paper on receptivity modelling

[...] adjoint eigensolutions act as a filter on a general disturbance field enabling to identify the amplitude of the corresponding eigenmode.

Combining the essences of both citations one might describe the boundary layer as a filter while the adjoint solution acts as its transfer function. Hence, projecting some given external disturbance field onto the adjoint solution of a certain eigenmode will yield its effective amplitude. This property, originally

demonstrated by Salwen & Grosch (1981), makes the adjoint solutions a powerful tool for receptivity prediction. Fedorov (1988) used adjoint solutions at finite Reynolds numbers to predict the receptivity of swept-wing boundary layers to surface roughness. An extensive study on how solutions to the adjoint Orr-Sommerfeld equations may be used to predict forced and natural receptivity in two-dimensional boundary layers was provided by Hill (1995). Later, he extended this technique and employed direct & adjoint PSE to account for nonparallel effects (Hill 1997). Similar methods were employed by Luchini & Bottaro (1998) to study the receptivity of Görtler vortices to free-stream and wall disturbances and by Airiau (2000) to describe acoustic scattering in a Blasius boundary layer. Pralits et al. (2000) employed the adjoint PSE for sensitivity analysis of compressible boundary layers. Dobrinsky & Collis (2000) and Dobrinsky (2002) considered direct & adjoint LNSE solutions as well as those of the PSE to predict the receptivity of various two- and three-dimensional boundary layers. Finally, Giannetti & Luchini (2006) combined adjoint solutions with an asymptotic approach to study the generation of Tollmien-Schlichting waves in the leading-edge region of an incompressible flat-plate boundary layer.

In order to predict the receptivity of crossflow modes in the swept-wing boundary layer we follow these works and define the adjoint through a Lagrange identity. The following derivation is performed for simple flat-plate geometries and based on direct and adjoint PSE solutions only. The corresponding derivation for general, spanwise invariant geometries on the basis of direct and adjoint LNSE solutions is presented in paper 4. Some results for a swept-wing boundary layer are shown in §5.3.

In order to be able to account for the receptivity to sources of mass and momentum, the PSE (4.24) are extended and become

$$\mathcal{L}_p \mathbf{q} = \mathbf{S},\tag{5.5}$$

where $\mathbf{S} = (S_m, \mathbf{S}_v)^T$ represents time- and spanwise-periodic sources of mass S'_m and momentum \mathbf{S}'_v respectively. The latter have the form $\mathbf{S}' = \mathbf{S}\Theta e^{i\beta z - i\omega t}$. The Lagrange identity defining the adjoint PSE becomes

$$\langle \mathbf{q}^*, \mathcal{L}_p \mathbf{q} - \mathbf{S} \rangle = \langle \mathcal{L}_p^* \mathbf{q}^*, \mathbf{q} \rangle + \iint_{\Omega} \nabla \cdot \mathcal{J}(\mathbf{q}, \mathbf{q}^*) \, dx dy - \langle \mathbf{q}^*, \mathbf{S} \rangle,$$
 (5.6)

where the inner product ' $\langle \cdot \rangle$ ' is defined as

$$\langle a, b \rangle = \iint_{\Omega} a^H b \, \mathrm{d}x \mathrm{d}y$$
 (5.7)

for some \mathbb{C}^n -valued functions a, b and Ω being an open bounded subset of \mathbb{R}^2 defined by the domain of interest. The superscript '*' denotes adjoint quantities. The term $\mathcal{L}_p \mathbf{q} - \mathbf{S}$ represents the direct inhomogeneous PSE. The adjoint equations are then defined as

$$\mathcal{L}_{p}^{*}\mathbf{q}^{*} = 0 \tag{5.8}$$

and $\mathcal{J} = (J_x, J_y)^T$ is known as the bilinear concomitant. Both \mathcal{L}^* and \mathcal{J} are obtained by performing integration by parts on the leftmost inner product of

(5.6). The adjoint operator of the PSE is then obtained as

$$\mathcal{L}_p^* = \mathbf{A}^* + \mathbf{B}^* \frac{\partial}{\partial y} + \mathbf{C}^* \frac{\partial^2}{\partial y^2} + \mathbf{D}^* \frac{\partial}{\partial x}, \tag{5.9}$$

with individual linear operators given by

$$\mathbf{A}^* = \mathbf{A}^H - \frac{\partial \mathbf{B}^H}{\partial y} - \frac{\partial \mathbf{D}^H}{\partial x} + \frac{\partial^2 \mathbf{C}^H}{\partial y^2}$$
 (5.10a)

$$\mathbf{B}^* = -\mathbf{B}^H + 2\frac{\partial \mathbf{C}^H}{\partial y} \tag{5.10b}$$

$$\mathbf{C}^* = \mathbf{C}^H \tag{5.10c}$$

$$\mathbf{D}^* = -\mathbf{D}^H. \tag{5.10d}$$

A, **B**, **C** and **D** refer to the PSE operators given in (4.26). The bilinear concomitant becomes

$$J_x = (\mathbf{q}^*)^H \mathbf{D} \mathbf{q} \tag{5.11a}$$

$$J_{y} = (\mathbf{q}^{*})^{H} \mathbf{B} \mathbf{q} + (\mathbf{q}^{*})^{H} \mathbf{C} \frac{\partial \mathbf{q}}{\partial y} - \frac{\partial (\mathbf{q}^{*})^{H}}{\partial y} \mathbf{C} \mathbf{q}.$$
 (5.11b)

If \mathbf{q} and \mathbf{q}^* are solutions to the direct PSE and adjoint PSE respectively, *i.e.* $\mathcal{L}_p \mathbf{q} - \mathbf{S} = \mathcal{L}_p^* \mathbf{q}^* = 0$, and if the boundary conditions $(u^*, v^*, w^*) = 0$ are imposed at the wall and in the free-stream the Lagrange identity (5.6) becomes

$$0 = \int_0^\infty \left[J_x \right]_{x_0}^{x_1} dy - \int_{x_0}^{x_1} \left[(\mathbf{q}^*)^H \mathbf{B} \mathbf{q} - \frac{\partial (\mathbf{q}^*)^H}{\partial y} \mathbf{C} \mathbf{q} \right]_{y=0} dx - \iint_{\Omega} (\mathbf{q}^*)^H \mathbf{S} dx dy.$$
 (5.12)

Here it was assumed, that the free-stream boundary is located far away from the boundary layer such that p^* as well as $\partial \mathbf{q}^*/\partial y$ have decayed to zero. Further, the function J_x is normalised such that

$$\tilde{J}_x = \frac{J_x}{A} \tag{5.13}$$

while the complex amplitude A is defined as

$$A(x) = \hat{u}(x, y_{max}), \tag{5.14}$$

and y_{max} is the position where |u| takes its maximum value. Introducing $\mathbf{q} = \Theta^{-1}\hat{\mathbf{q}}$ and $\mathbf{S} = \Theta^{-1}\hat{\mathbf{S}}$ the Lagrange identity can be recast into

$$A(x_1) \int_0^\infty \tilde{J}_x(x_1) \, \mathrm{d}y = A(x_0) \int_0^\infty \tilde{J}_x(x_0) \, \mathrm{d}y$$

$$+ \int_{x_0}^{x_1} \Theta^{-1} \left[(\mathbf{q}^*)^H \mathbf{B} \hat{\mathbf{q}} - \frac{\partial (\mathbf{q}^*)^H}{\partial y} \mathbf{C} \hat{\mathbf{q}} \right]_{y=0} \, \mathrm{d}x \quad (5.15)$$

$$+ \iint_{\Omega} \Theta^{-1} (\mathbf{q}^*)^H \hat{\mathbf{S}} \, \mathrm{d}x \, \mathrm{d}y.$$

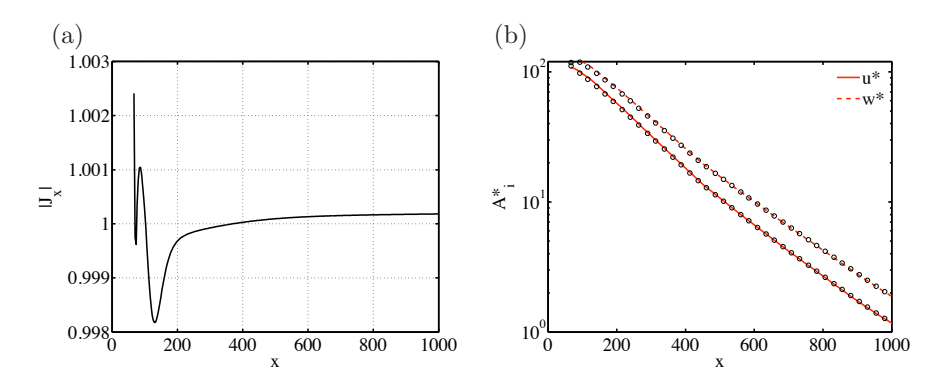


FIGURE 5.3. (a) The absolute value of J_x , normalised with its mean, versus x. (b) Adjoint solution for a crossflow mode with $\beta=0.19,\,\omega=0$ obtained by solving the PSE (—) and by DNS (o). A_i^* denotes the wall-normal maximum of either $|u^*|$ or $|w^*|$.

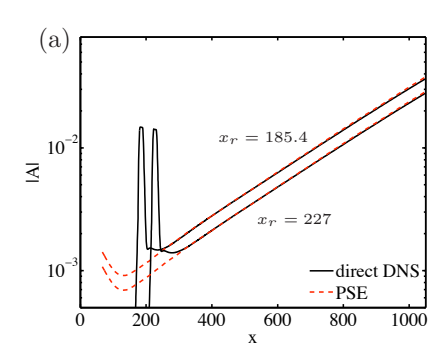
This equation may be used to predict the receptivity to wall disturbances $\hat{\mathbf{q}}(y=0)$, inflow disturbances $\hat{\mathbf{q}}(x_0)$ or mass and momentum sources $\hat{\mathbf{S}}$. Assuming that neither inhomogeneous boundary conditions at the wall nor mass or momentum sources change the shape of the mode of interest but just its amplitude and phase, $\tilde{J}_x(x_1)$ can be evaluated on the basis of the homogeneous solution to the direct & adjoint PSE for the modal disturbance of interest. The term 'homogeneous' here refers to solutions obtained for zero-slip wall-boundary conditions and zero mass or momentum sources.

It is worth to note that J_x represents a conserved quantity for the homogeneous case, *i.e.* when the second and third term of the right-hand-side of (5.15) are zero. This property is useful when evaluating the accuracy of the direct & adjoint PSE and can be related to the orthogonality of direct and adjoint eigenmodes (see Dobrinsky 2002, for more details). Figure 5.3(a) shows J_x versus x for the current computations of a steady crossflow mode with $\beta=0.19$. It is apparent that J_x is well conserved. The maximum difference from the mean value of J_x is about 0.2%. Solutions to the direct & adjoint PSE are therefore found to be sufficiently accurate. This is confirmed by results shown in figure 5.3(b). Respective solutions of the adjoint PSE and adjoint LNSE are in perfect agreement.

5.2.1. Receptivity to surface roughness

Disregarding any mass or momentum sources the receptivity amplitude of the disturbance at x_1 is given by

$$A(x_1) = \frac{1}{\int_0^\infty \tilde{J}_x(x_1) \,dy} \int_{x_0}^{x_1} \Theta^{-1} \left[(\mathbf{q}^*)^H \mathbf{B} \hat{\mathbf{q}} - \frac{\partial (\mathbf{q}^*)^H}{\partial y} \mathbf{C} \hat{\mathbf{q}} \right]_{y=0} \,dx. \quad (5.16)$$



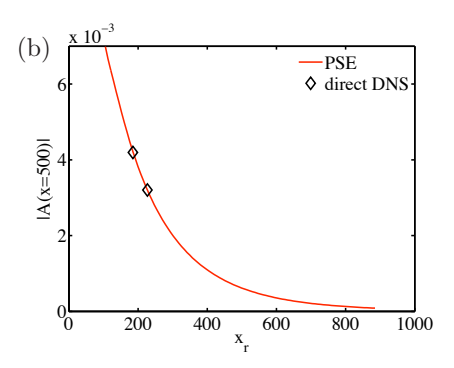


FIGURE 5.4. (a) Boundary layer response to surface roughness as predicted by DNS and the PSE-based receptivity model. (b) Receptivity amplitudes at x=500 as predicted by DNS and the PSE-based receptivity model.

It is assumed that the amplitude of the incoming disturbance is $A(x_0) = 0$. Equation (5.16) allows to predict the receptivity of a boundary layer to inhomogeneous boundary conditions. Hence, considering the roughness model (5.1) it is possible to predict the boundary layer response to surface roughness. Introducing the roughness model and evaluating the right-hand side (5.16) yields

$$A(x_1) = -\frac{1}{Re \int_0^\infty \tilde{J}_x(x_1) \, \mathrm{d}y} \int_{x_0}^{x_1} \Theta^{-1} H_\beta \left[\frac{\partial \bar{u}^*}{\partial y} \frac{\partial U}{\partial y} + \frac{\partial \bar{w}^*}{\partial y} \frac{\partial W}{\partial y} \right]_{y=0} \, \mathrm{d}x,$$
(5.17)

where an overbar means complex conjugate. The crossflow mode amplitudes predicted on the basis of (5.17) are depicted in figure 5.4. The roughness shape presented in §5.1.1 is considered and results are compared to the respective direct LNSE solutions. The agreement between the PSE-based prediction and the response obtained by solving the direct LNSE is excellent. The receptivity amplitudes for arbitrary roughness positions can be easily obtained by changing the roughness model in (5.17). Note, that no further direct & adjoint PSE solutions are required as long as the receptivity amplitudes of the same crossflow mode are to be determined. It is apparent from figure 5.4 that the receptivity amplitude for a crossflow mode with $\beta=0.19$ extracted at x=500 decreases monotonically for roughness positions farther downstream. Again, the comparison to the direct LNSE solutions shows perfect agreement. Hence, PSE-based receptivity prediction employing direct and adjoint PSE solutions is perfectly suited for modelling the boundary layer response to micron-sized, localised surface roughness.

$5.2.2.\ Receptivity\ to\ free-stream\ disturbances$

The receptivity to initial free-stream disturbances $\mathbf{q}(x_0)$ is studied by considering equation (5.15) for homogeneous wall-boundary conditions and zero sources.

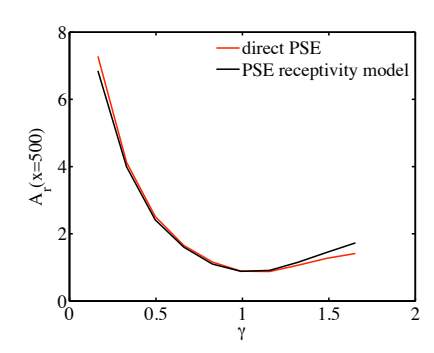


FIGURE 5.5. Receptivity amplitude of the boundary layer response to initial vortical free-stream disturbances as predicted by direct PSE and the PSE-based receptivity model. Steady vorticity modes (Mode A) of the continuous spectrum with $\gamma \in [0.165, 1.65]$ and $\beta = 0.19$ are considered.

The receptivity amplitude is then obtained as

$$A(x_1) = A(x_0) \frac{\int_0^\infty \tilde{J}_x(x_0) \, dy}{\int_0^\infty \tilde{J}_x(x_1) \, dy}.$$
 (5.18)

Now, $\tilde{J}_x(x_0)$ is evaluated on the basis of the initial free-stream disturbance $\mathbf{q}(x_0)$ while $\tilde{J}_x(x_1)$ is known from the homogeneous solutions of the modal disturbance. As in §5.1.2, receptivity is quantified by the normalised amplitude A_r which is defined as

$$A_r(x_1) = \left| \frac{A(x_1)}{A(x_0)} \right|. (5.19)$$

The receptivity prediction obtained by evaluating (5.18) for those vortical freestream modes considered already in §5.1.2 is presented in figure 5.5. The predicted receptivity amplitudes are compared to the respective boundary layer response obtained from the direct PSE solution (cf. figure 5.2 b). Again, the performance of the PSE-based receptivity model is found to be very satisfying as the predicted amplitudes are very close to those obtained from the direct PSE computations.

5.2.3. Optimal excitation of modal disturbances

If no information on the external disturbance environment is given, the receptivity of a boundary-layer flow may also be studied by considering the worst-case scenario, *i.e.* the so-called optimal disturbance. The latter is defined through maximum spatial growth. If the boundary layer exhibits a dominant mode which the flow is always attracted to sufficiently far downstream, the optimal initial disturbance of the flow will yield a maximum receptivity amplitude A_r of this dominant mode. Since $\tilde{J}_x(x_1)$ is computed on the basis of the eigenmode of interest, its optimal initial disturbance $\mathbf{q}_{opt}(x_0)$ is obtained by maximising

 $\int_0^\infty \tilde{J}_x(x_0) \,\mathrm{d}y$ (cf. equation 5.18). Recalling the definition of J_x in (5.11), a maximum receptivity coefficient is obtained by maximising the projection of \mathbf{q} on $(\mathbf{D}^H \mathbf{q}^*)$. This is obtained by choosing

$$\mathbf{q}(x_0) = \mathbf{D}^H \mathbf{q}^* \bigg|_{x_0}. \tag{5.20}$$

which in detail reads

$$u(x_0) = p^* + Uu^*|_{x_0}$$
 (5.21a)

$$v(x_0) = Uv^*|_{x_0}$$
 (5.21b)

$$w(x_0) = Uw^*\Big|_{x_0} \tag{5.21c}$$

$$p(x_0) = u^*|_{x_0}.$$
 (5.21d)

It becomes apparent that a choice according to (5.21) would not yield a physical disturbance though since the adjoint equations do not involve a boundary condition for p^* at the wall. Hence, (5.21a) would yield a non-physical optimal disturbance component $u(x_0)$. Here, we follow the approach outlined in paper 1, where p^* is neglected in the sum (5.21a). Results presented in paper 1 show that this does not have measurable effects on the optimal growth. Also the optimal choice for $p(x_0)$ does not necessarily yield a physical disturbance since no constraints on the initial disturbance are imposed. However, since the pressure gradient term $\partial p/\partial x$ is neglected in the PSE there is no need to prescribe an initial pressure profile. Hence, the optimal initial disturbance is chosen as

$$u(x_0) = Uu^*|_{x_0}$$
 (5.22a)
 $v(x_0) = Uv^*|_{x_0}$ (5.22b)

$$v(x_0) = Uv^*$$
 (5.22b)

$$w(x_0) = Uw^* \Big|_{x_0}. (5.22c)$$

The corresponding initial disturbance shape at $x_0 = 67$ which optimally excites a steady crossflow mode with $\beta = 0.19$ is shown in figure 5.6. It is apparent from figure 5.6 (a) that the initial optimal disturbance is characterised by dominant crossflow- and wall-normal disturbance velocity components w_s and v. It takes the form of streamwise tilted vortices. However, the streamwise component u_s , though less in amplitude, is of similar order and thus not negligible as opposed to the case of two-dimensional boundary layers. The receptivity amplitude at x = 500 predicted based on equation (5.18) is $A_r = 64.17$. This prediction is compared with a direct PSE computation where (5.22) is chosen as the initial disturbance at x_0 . Note that this direct PSE was solved employing the second choice of closure with respect to α as described in §4.2.2. Hence, α was determined globally on the basis of 4.33). The optimal boundary-layer response predicted by the PSE-based receptivity model is in perfect agreement to the result of the direct PSE (see figure 5.7). By comparing the spatial evolution of the optimal disturbance with that of a clean crossflow mode an initial region of strong non-modal growth becomes apparent. Farther downstream, i.e. for x > 200, the optimal disturbance smoothly evolves into the dominant crossflow

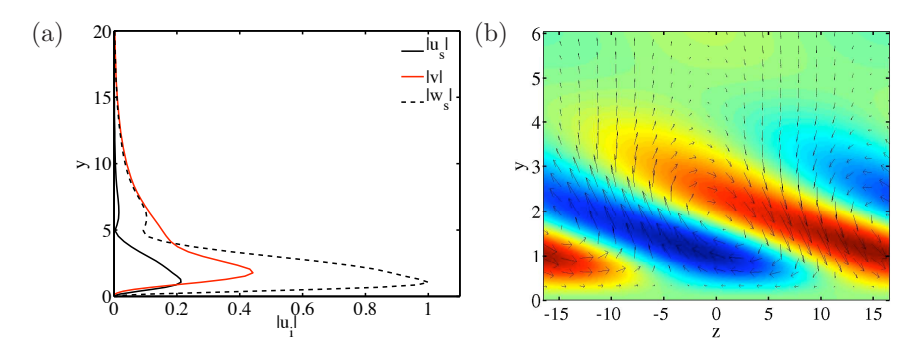


FIGURE 5.6. Optimal initial disturbance at $x_0 = 67$ for a crossflow mode with $\beta = 0.19$ and $\omega = 0$. (a) Shape functions of disturbance velocity components projected onto a plane perpendicular to the external streamline direction. (b) Pseudocolors of u_s and vectors denoting (v, w_s) .

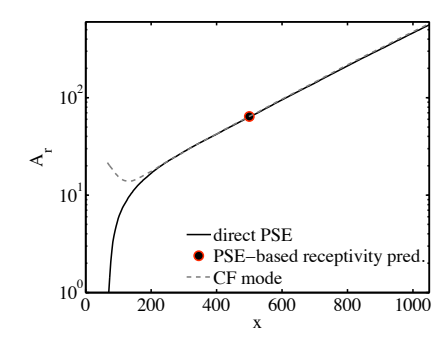


FIGURE 5.7. Spatial evolution of steady optimal disturbance with $\beta=0.19$ compared with the evolution of a clean crossflow mode as well as the PSE-based receptivity prediction at x=500.

mode. Additional details on spatial optimal growth, in particular for regions of the boundary layer where no dominant mode exists, are given in the next chapter.

$5.2.4.\ Receptivity\ to\ spanwise-periodic,\ time-harmonic\ sources$

Finally, the receptivity to sources of mass and momentum is considered. Assuming a smooth wall and no incoming disturbances, *i.e.* $A(x_0) = 0$, equation (5.15) becomes

$$A(x_1) = \frac{1}{\int_0^\infty \tilde{J}_x(x_1) \,dy} \iint_\Omega \Theta^{-1}(\mathbf{q}^*)^H \hat{\mathbf{S}} \,dx \,dy$$
 (5.23)

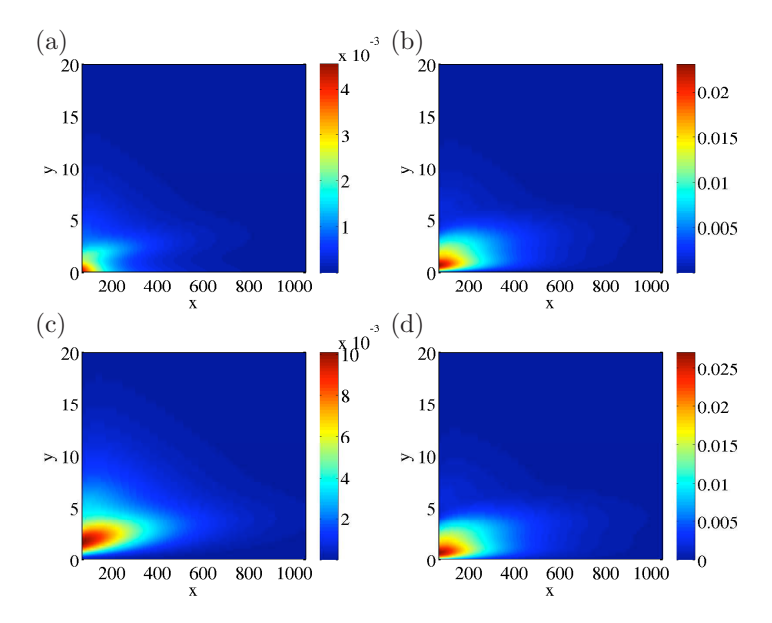


FIGURE 5.8. Optimal distribution of sources of mass (a) and x-,y- and z-momentum (b,c,d) for a steady crossflow mode with $\beta=0.19$. Pseudocolors of the respective source amplitudes are shown where $\hat{\mathbf{S}}$ was normalised such that $\left\langle \hat{\mathbf{S}}, \hat{\mathbf{S}} \right\rangle=1$.

The optimal source distribution yielding a maximum receptivity amplitude of the crossflow mode of interest is then obtained by maximising the integral term in equation (5.23). Accordingly, the choice

$$\hat{\mathbf{S}} = \bar{\Theta}^{-1} \mathbf{q}^* \tag{5.24}$$

yields the optimal response of a boundary layer to distributed sources of mass and momentum. The optimal sources presented in figure 5.8 are normalised such that $\langle \hat{\mathbf{S}}, \hat{\mathbf{S}} \rangle = 1$. All sources have a maximum amplitude at the inflow. Farther downstream the amplitude decreases monotonically. The wall-normal position of the maximum amplitude is closely related to the wall-normal maximum of the corresponding crossflow mode shape. The optimal forced boundary layer response may be quantified by a normalised amplitude of the form

$$A_s = \frac{|A(x_1)|}{\left\langle \hat{\mathbf{S}}, \hat{\mathbf{S}} \right\rangle}.$$
 (5.25)

In this case, for a steady crossflow mode with $\beta=0.19$, the optimal forced response amplitude at x=500 predicted based on (5.23) is $A_s=434$.

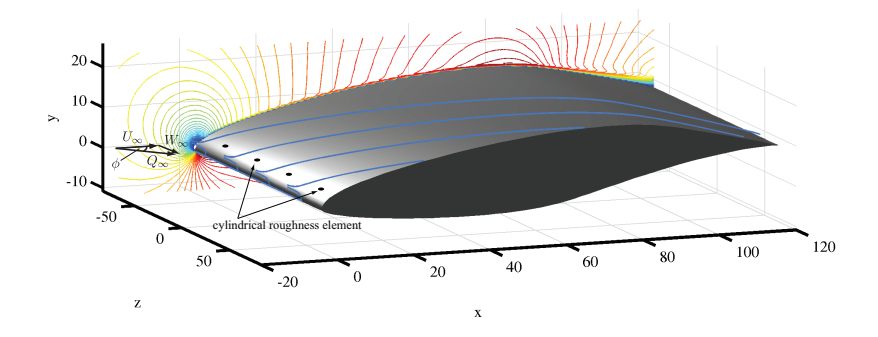


FIGURE 5.9. Geometry of the swept wing (NLF(2)-0415 airfoil, Somers & Horstmann 1985) which is at an angle of attack of -4° . The sweep angle is $\phi = 45^{\circ}$. The coloured contours denote the meanflow while blue lines represent the respective streamlines.

5.3. Receptivity of a swept-wing boundary layer

The adjoint-based receptivity theory presented in the previous section can be generalised to become applicable to more complex geometries such as a sweptwing boundary layer. In particular, evaluating the Lagrange identity (5.6) on the basis of the LNSE instead of the PSE allows to study additional receptivity mechanisms, i.e. the receptivity to free-stream disturbances upstream of a swept wing. Such generalisations are the topic of papers 3 & 4. Here, the potentials of adjoint-based receptivity prediction shall be demonstrated by presenting a few baseline results. The flow case is a swept-wing boundary layer which conforms to experiments by Saric & coworkers at Arizona State University in the 1990's (see e.g. Reibert et al. 1996). The wing is at an angle of attack of -4° while the sweep angle is $\phi = 45^{\circ}$. This choice yields a favourable pressure gradient on the upper wing side and results in a strong crossflow instability. The wing geometry, which is invariant in the spanwise direction, is depicted in figure 5.9. In order to predict the receptivity of the swept-wing boundary layer to localised surface roughness as well as steady freestream disturbances the adjoint LNSE are solved for the most unstable steady crossflow mode. The adjoint solution, which is depicted in figure 5.10, has a very interesting shape. Inside the boundary boundary layer it is strongest close to the wall and increases in amplitude towards the stagnation region of the meanflow. It exhibits very thin structures that require a high resolution. Upon approaching the stagnation region the adjoint solution extends into the freestream upstream of the leading edge where it becomes strongly damped. In the free-stream it is very localised and well aligned with the meanflow streamlines. A spanwise cut of the adjoint solution as well as its modal amplitudes in the free-stream at x = -10 are shown in figure 5.11. It is important to note the u_s^* -component, which is in the direction of the incoming homogeneous

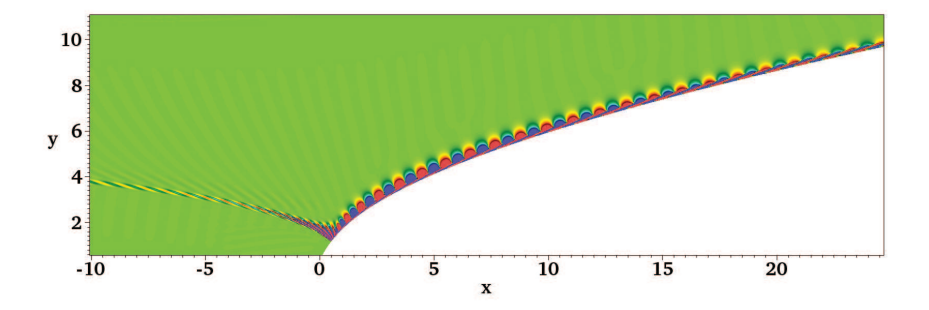


FIGURE 5.10. Adjoint solution u^* (blue: negative; red: positive) of a steady crossflow mode with $\beta=5.6523$ in a sweptwing boundary layer extending into the free-stream upstream of the leading edge.

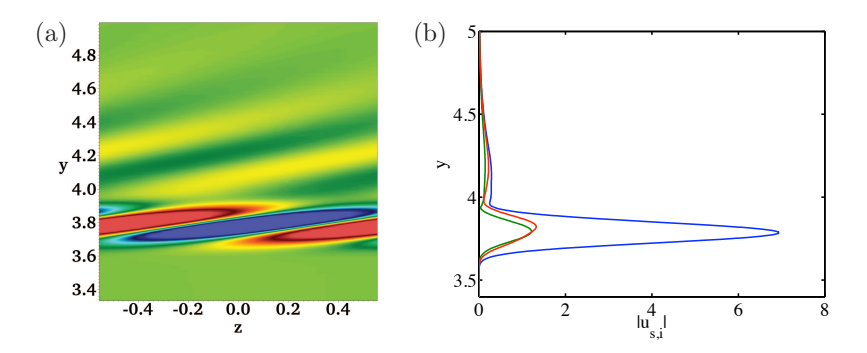


FIGURE 5.11. (a) Spanwise cut in the free-stream at x=-10 of the adjoint solution u^* of a steady crossflow mode with $\beta=5.6523$. (b) The respective modal amplitudes of $u_s^*(-), v^*(-)$ and $w_s^*(-)$. The subscript 's' denotes projection on to a plane which is perpendicular to the direction of the incoming free-stream. Hence u_s^* is in the direction of Q_{∞} (cf. figure 5.9).

flow, clearly dominates over v_s^* and w_s^* . Receptivity amplitudes of the steady crossflow mode can now be obtained by projecting external disturbances on to the adjoint solution. Paper 3 discusses the receptivity of this boundary layer to localised, micron-sized circular roughness cylinders as depicted in 5.9. The latter may be modelled by inhomogeneous boundary conditions (cf. equation 5.1). For a specific definition of the roughness it is referred to paper 3. Receptivity amplitudes are then easily obtained by projecting the respective velocities at the wall onto the adjoint solution (by employing a relation similar to equation 5.17). Receptivity amplitudes of the steady crossflow mode, which are obtained for different roughness positions, are presented in figure 5.12. The predictions

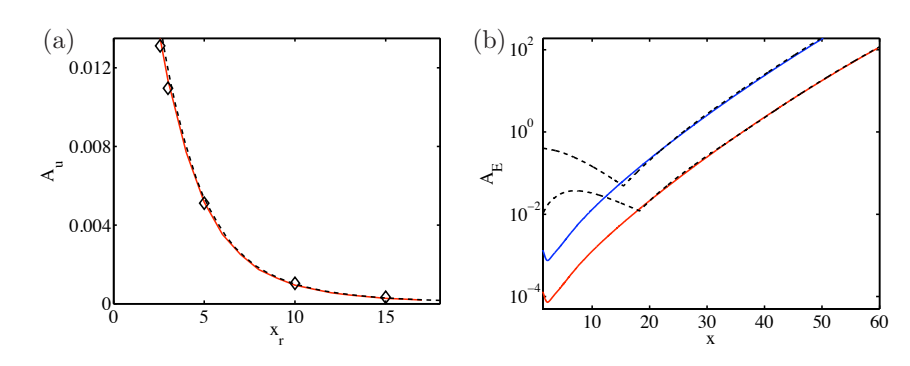


FIGURE 5.12. Receptivity amplitudes predicted by projecting external disturbances on to the adjoint solution of a steady crossflow mode with $\beta=5.6523$. (a) Receptivity to localised circular roughness cylinders as predicted on the basis of the adjoint LNSE (—), the adjoint PSE (---) and direct solutions of the LNSE where the roughness was meshed (\diamond). (b) Receptivity to streamwise (—) and vertical (—) free-stream vorticity. Solid lines denote prediction based on the adjoint LNSE while dashed lines represent a direct LNSE solution.

obtained on the basis of both adjoint LNSE and adjoint PSE agree perfectly with the response, which is obtained from a direct LNSE solution. The latter featured meshed roughness elements.

Something which is not possible with the PSE is to predict the receptivity to free-stream disturbances upstream of the leading edge. However, by employing the adjoint LNSE solution presented in figure 5.11 this becomes possible. Tempelmann et al. (2011) studied the receptivity of the same swept-wing boundary layer to free-stream vorticity by means of direct LNSE. Hence for each individual vorticity mode one simulation was needed. Based on the adjoint solution presented here it is possible to accurately predict the receptivity amplitude of the respective crossflow mode to any free-stream disturbance. This is demonstrated in figure 5.12 (b) where the adjoint-based amplitude predictions are compared with the direct LNSE results by Tempelmann et al. (2011). As in the roughness case the agreement is perfect. The initial discrepancy is because of the dominant free-stream disturbances present in the direct LNSE which covers the the present crossflow mode. Further downstream the crossflow mode becomes dominant and perfectly agrees with the adjoint-based prediction. It is apparent that vertical vorticity is more efficient in exciting steady crossflow disturbances than streamwise vorticity. This observation is easily explained by recalling the dominance of the u_s^* -component of the adjoint solution. When projecting on to the adjoint solution the streamwise u_s -component of the freestream disturbance is multiplied with u_s^* . Since streamwise vorticity implies a

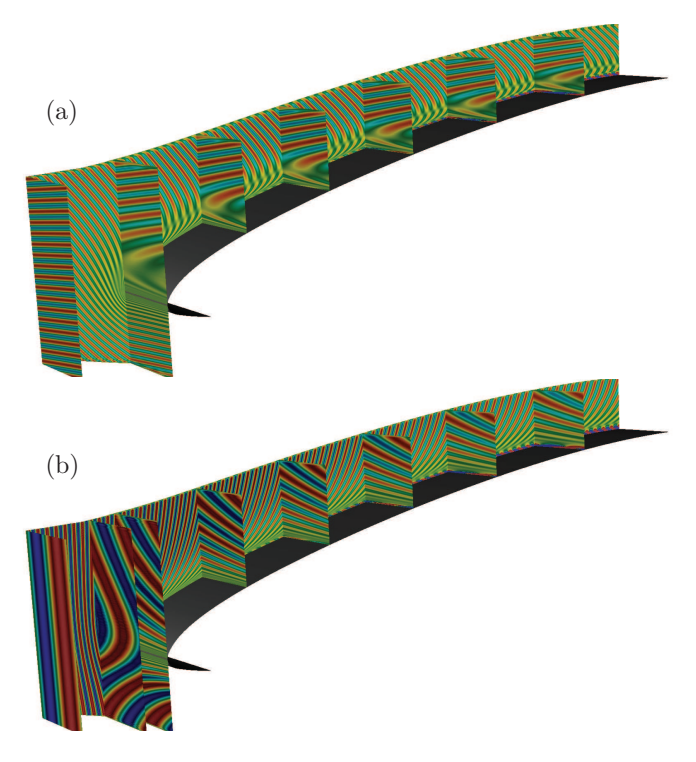


FIGURE 5.13. Response of the swept-wing boundary layer to (a) streamwise and (b) vertical vorticity as obtained by solving the direct LNSE. Red and blue pseudocolors denote positive and negative *u*-disturbance velocities respectively. For details it is referred to Tempelmann *et al.* (2011).

zero streamwise velocity component the corresponding receptivity is found to be weaker as compared with vertical vorticity.

The direct LNSE solutions are shown in figure 5.13. Most striking is the influence of the stagnation region on the disturbance evolution in both cases. While approaching the stagnation line, chordwise velocities become damped. Hence, close to the stagnation line disturbances are mainly convected in the spanwise direction. This results in stretching and tilting of the vorticity which is nicely depicted in figure 5.13 (b). Farther downstream, close to the wall, the crossflow mode becomes visible in both cases.

CHAPTER 6

Spatial non-modal & optimal growth

The receptivity analysis presented in the previous section deals with how to optimally excite a certain eigenmode. If such a mode is dominant, i.e. the flow is always attracted to it, it represents the optimal disturbance. However, in those regions of the flow which are subcritical with respect to modal growth all modal disturbances decay and no such dominant mode exists. Nonetheless, transient disturbance growth may be observed. Mathematically, this is due to the non-normality of the governing linear operator. A detailed discussion may be found in Trefethen et al. (1993); Schmid & Henningson (2001) and Schmid (2007). Non-modal disturbances in the form of streaks were first observed in an experiment by Klebanoff (1971) who studied a two-dimensional boundary layer subject to free-stream turbulence. Streaks are disturbances elongated in streamwise direction which are characterised by alternating high and low speed flow. The physical mechanism behind this phenomenon is the so-called 'lift-up effect' which was first formulated by Landahl (1980). Fluid particles keeping their horizontal momentum when being displaced vertically because of streamwise vorticity lead to the formation of streamwise perturbations; the so-called streaks. The optimal spatial growth of these disturbances was first studied by Andersson et al. (1999) and Luchini (2000) for the Blasius boundary layer. In the following it is shown how spatial optimal growth may be studied in the three-dimensional FSC boundary layer. As opposed to the method in §5.2.3 the presented method may be employed in the subcritical boundary layer, i.e. where it is stable to crossflow disturbances.

By employing a temporal framework Corbett & Bottaro (2001) found non-modal disturbances and crossflow modes to be of similar structure in three-dimensional boundary layers. Hence, the PSE, which have been found to perfectly describe the spatial evolution of crossflow disturbances, are assumed to also represent a valid approximation for the spatial growth of non-modal disturbances. However, in order to be able to describe the evolution of general disturbances in the FSC boundary layer the PSE are solved by determining α globally based on (4.33). In this section, an optimal disturbance is associated with maximum spatial energy growth. Hence the objective function to be

maximised takes the form

$$J(\mathbf{q}) = \frac{\int_0^\infty \mathbf{q}^H M \mathbf{q} \, dy \Big|_{x_1}}{\int_0^\infty \mathbf{q}^H M \mathbf{q} \, dy \Big|_{x_0}}$$
(6.1)

with M = diag(1,1,1,0) and (x_0,x_1) denoting the initial position and the position of maximum amplification respectively. Note, that in order for (6.1) to represent disturbance energy growth α needs to be chosen real-valued. Then the disturbance growth is captured by \mathbf{q} instead of by the phase function (cf. §4.2.2). Maximising $J(\mathbf{q})$ represents a constrained optimisation problem since \mathbf{q} is required to satisfy the governing equations which in this case are the PSE (4.24). Having chosen the objective function the method of Lagrange multipliers can be employed and the Lagrange functional takes the form

$$\mathcal{L}(\mathbf{q}, \mathbf{q}^*) = J(\mathbf{q}) - \langle \mathbf{q}^*, \mathcal{L}_p \mathbf{q} \rangle. \tag{6.2}$$

Note, that in this section we redefine the inner product according to $\langle \cdot \rangle = \langle \cdot \rangle + c.c.$ to ensure a real-valued functional. The adjoint state vector \mathbf{q}^* here takes the role of a Lagrange multiplier enforcing \mathbf{q} to satisfy the governing equations. The maximum of $J(\mathbf{q})$ is now obtained by finding the stationary points of (6.2) which are the roots of the first variation of \mathcal{L} . Hence, it is required that

$$\delta \mathcal{L} = \langle \nabla_{\mathbf{q}^*} \mathcal{L}, \delta \mathbf{q}^* \rangle + \langle \nabla_{\mathbf{q}} \mathcal{L}, \delta \mathbf{q} \rangle = 0, \tag{6.3}$$

where $\nabla_{\mathbf{q}}$ represents a gradient with respect to \mathbf{q} . To obtain the roots both inner products in (6.3) have to render zero independently. Setting the first inner product to zero implies solving the PSE, *i.e.* $\mathcal{L}_p \mathbf{q} = 0$. The second inner product becomes zero if $\nabla_{\mathbf{q}} \mathscr{L} = 0$. This gradient is most easily obtained by adopting the Lagrange identity (5.6) where \mathbf{S} is considered to be zero in this case. The adjoint state \mathbf{q}^* is assumed to be a solution of the adjoint PSE $\mathcal{L}_p^* \mathbf{q}^* = 0$. Further, zero Dirichlet boundary conditions are imposed for both (u^*, v^*, w^*) and (u, v, w) at the wall and in the free-stream. Under these conditions, only terms stemming from the gradient of the objective function, $\nabla_{\mathbf{q}} J$, and the x-component of the bilinear concomitant (5.11a) are left in the second inner product of (6.3). The first variation of $\mathscr L$ then turns into

$$\mathbf{D}^H \mathbf{q}_k^* - c_k M \mathbf{q}_k = 0, \tag{6.4}$$

where c represents a normalisation coefficient and k denotes both boundaries x_0 and x_1 . Equation (6.4) represents the so-called optimality conditions which have to be fulfilled at either boundaries in order to maximise (6.1) and which, at x_0 yield the optimal initial disturbance. As discussed in §5.2.3 the adjoint pressure is neglected in (6.4) since it does not comprise a boundary condition at the wall and leads to an unphysical initial disturbance. This leads to an optimal initial disturbance of the form (5.22). The complete optimality system is solved iteratively starting with an arbitrary initial guess for $\mathbf{q}(x_0)$.

Employing the above described optimisation to the FSC boundary layer optimal disturbances can be computed for various parameters. In figure 6.1

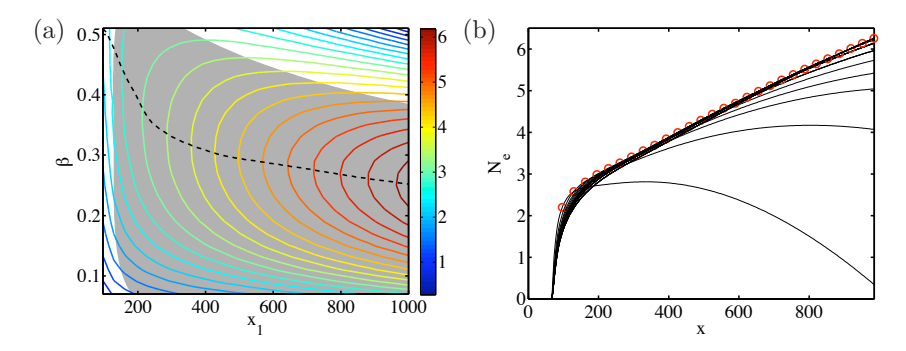


FIGURE 6.1. (a) Pseudocolors of N-factors of steady optimal disturbances impinging at $x_0=67$. The grey region denotes the boundary layer regime which is unstable to modal cross-flow disturbances (cf. figure 4.8). The dashed line denotes the optimal spanwise wavenumber $\beta_{opt}(x_1)$. (b) N-factors of energy growth of optimal disturbances with optimal $\beta_{opt}(x_1)$ extracted from plot (a). Red circles denote the spatial optimal growth $J(x_1)$ at the respective position of maximum amplification

the spatial growth of steady optimal disturbances is presented versus β and the position of maximum amplification x_1 . Note that spatial growth is quantified in terms of energy N-factors

$$N_e = 0.5 \ln \left(\frac{E(x_1)}{E(x_0)} \right) \tag{6.5}$$

with $E = \langle \mathbf{q}, M\mathbf{q} \rangle$. It is apparent that the maximum N-factors obtained reach a value of $N_e \approx 6$ at the downstream boundary of the domain of interest. These are significantly higher than those N-factors obtained from the modal PSE analysis presented in figure 4.9. Note also, that even in regions close to and upstream of the neutral curve N-factors of $N_e=1$ to Ne=3 are obtained. Hence, even if the boundary layer is stable to modal crossflow instabilities, significant non-modal growth is observed. Based on the parametric data presented in figure 6.1(a) one may extract the optimal spanwise wavenumber $\beta_{opt}(x_1)$ of those disturbances exhibiting maximum optimal growth at each chordwise position x_1 . It becomes clear that the optimal spanwise length scales of the corresponding disturbances increase with increasing x_1 . The N-factors of these are shown in figure 6.1(b) versus the chordwise position x. Those disturbances exhibiting maximum optimal growth at small x_1 experience strong initial nonmodal growth and decay further downstream as opposed to the perturbations experiencing maximum growth at position farther downstream. The latter are also characterised by initial non-modal growth but turn into strongly growing crossflow modes farther downstream.

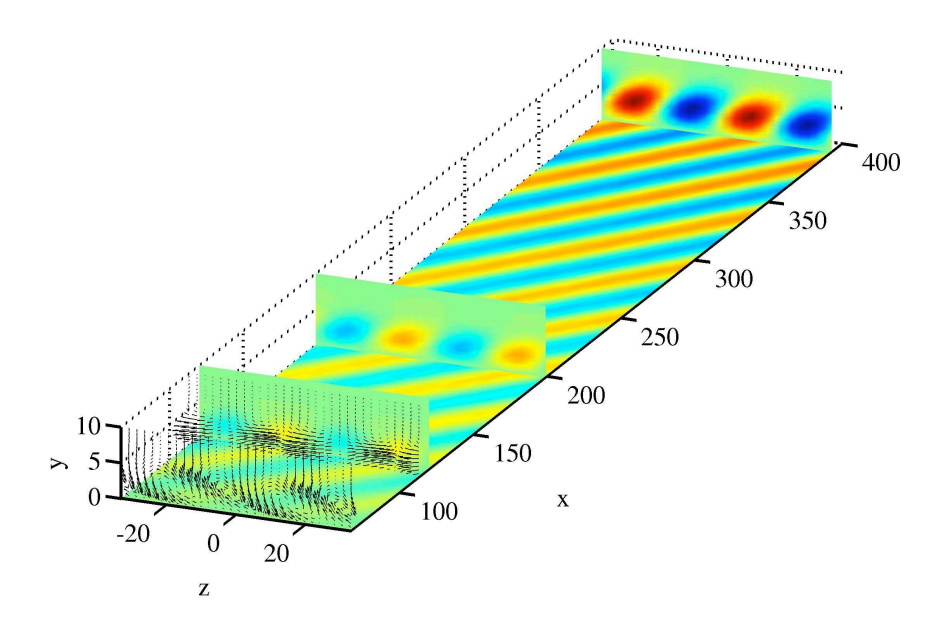


FIGURE 6.2. Optimal disturbance with $\beta = 0.19$, $\omega = 0$, $x_0 = 67$ and $x_1 = 400$ in physical space. For visualisation purposes the horizontal slice is shifted from y = 1.3 to the wall.

Examining the spatial structure of optimal disturbances in threedimensional boundary layers reveals a dominant initial vortical structure (cf. figure 6.2) as stated already in §5.2.3. These streamwise vortices are tilted against the direction of the mean crossflow shear. While evolving downstream the vortices rise up and turn into strongly growing boundary layer streaks. These structures thus point to the presence of two physical mechanisms of nonmodal growth, namely the Orr-mechanism and the lift-up mechanism. The Orr-mechanism, originally formulated by Orr (1907), describes how disturbances which are tilted against the baseflow shear extract energy through the action of a perturbation Reynolds stress while being erected. The lift-up mechanism was initially described by Landahl (1980) and relates initial vortical disturbances to the appearance of boundary layer streaks. The vortical motion displaces fluid particles vertically and, because of the streamwise baseflow shear, leads to horizontal perturbations in the form of streaks. In paper 1 it is shown that these non-modal streaks strongly resemble the structure of crossflow disturbances. Farther downstream they smoothly turn into crossflow disturbances as shown in figure 5.7. In conclusion, it is found that the FSC boundary layer

shows a significant potential for growth of non-modal disturbances which may be seen to initiate modal crossflow disturbances. Since both free-stream turbulence and roughness elements may excite disturbances of similar structure, non-modal growth can be related to a receptivity mechanism in 3D boundary layers. A comprehensive parametric study on spatial optimal growth in both incompressible and compressible swept-flat-plate boundary layers is presented in papers $1\ \&\ 2$.

CHAPTER 7

Stabilisation by localised roughness

All methods presented so far help to understand the physical mechanisms of disturbance generation and their evolution in boundary layers and provide quantitative predictions. However, the ultimate goal is to control these disturbances in such a way as to obtain a predominantly laminar boundary layer. The most obvious approach might be to choose a geometry which favourably affects the disturbance evolution. A systematic approach for such a shape optimisation has been developed by Amoignon et al. (2006). However, since various disturbance types react differently to changes in e.q. pressure gradient or surface curvature while at the same time requirements with respect to e.g. lift have to be met, the control parameters of this approach are limited. An active control approach which has been studied experimentally by Bippes (1999) is to apply surface suction. This mainly decreases the crossflow and thus attenuates the growth of crossflow disturbances. However, the experimental investigations showed that imperfections with respect to periodicity of the suction holes may lead to excitation of unstable non-stationary instabilities. This was confirmed numerically by Messing & Kloker (2010). Optimal spanwise homogeneous suction distributions for infinite swept wings were computed by Pralits & Hanifi (2003). Both Tollmien-Schlichting and crossflow instability waves could be stabilised.

A rather simple passive control mechanism has been initially proposed and studied by Saric et al. (1998a). These authors performed wind tunnel experiments to study the transition of a swept wing boundary layer. They showed that transition can be delayed significantly by artificially triggering a stationary crossflow disturbance which is subcritical with respect to transition. In the experiments this subcritical disturbance was triggered by placing a periodic array of circular roughness cylinders close to the leading edge. The spacing was chosen to correspond to a wavelength smaller than that of the naturally most unstable stationary crossflow disturbance. Such relatively small-scale disturbances are known to exhibit strong growth close to the leading edge and to decay farther downstream as opposed to disturbances of larger spanwise length scales. The latter are stable initially but grow strongly downstream.

Similar investigations were performed numerically by Wassermann & Kloker (2002) for a swept-flat-plate boundary layer. In accordance with the experimental observations by Saric & coworkers they found that the excitation of crossflow disturbances, which are subcritical with respect to transition, leads to nonlinear attenuation of the naturally most unstable disturbances. They

further explain that nonlinear effects lead to a strong meanflow modification that favourably affects the stability of the most unstable crossflow modes.

Here, the effects of subcritical forcing shall be briefly discussed using DNS solutions¹ of the FSC boundary layer introduced in §3. Only effects on the spatial evolution of stationary crossflow disturbances will be considered. Effects on the transition of a swept-wing boundary layer, which corresponds to the experiments by Saric *et al.* (1998*a*), is presented in paper 5.

In the FSC boundary layer the most unstable steady crossflow instabilities exhibit wavenumbers $\beta \approx 0.2$ towards the end of the considered domain. It is these crossflow disturbances that shall be damped in the following. Accordingly, the mode with $\beta_t = 0.2$ is chosen to be the *target* mode. In order to make this example more realistic a very simple model for natural roughness is introduced by considering a roughness element localised in x having the form

$$h(x,z) = \epsilon_h H_{\beta}(x) \sum_{k=1}^{6} \sin(k\beta_0 z + \varphi_{r,k}). \tag{7.1}$$

Here, H_{β} denotes the roughness shape defined in (5.3), β_0 denotes the fundamental mode defined by the width of the computational box. The phase $\varphi_{r,k}$ is chosen randomly for each mode. Hence, this surface roughness will excite multiple steady crossflow instabilities of random phase with spanwise wavenumbers $k\beta_0$ and k ranging from 1, 2, ..., 6. The box width and thus the fundamental mode are chosen such that both the target mode and the subcritical mode aimed at controlling the latter, denoted the 'control' mode, can be considered. Saric et al. (1998a) chose the spanwise wavenumber of the control mode to be 3/2 of the target mode wavenumber. Wassermann & Kloker (2002) found this choice to be optimal. Accordingly, the fundamental wavenumber is chosen as $\beta_0 = \beta_t/2 = 0.1$ corresponding to a box size $L_z = 2\pi/\beta_0 = 62.83$. The control mode then has the wavenumber $\beta_c = 0.3$. The 'natural' roughness is located at $x_r = 185.4$ while $\epsilon_h = 0.0032$. The control mode is triggered farther downstream by a second row of roughness elements as shown in figure 7.1. This 'control' roughness is located at $x_r = 280.8$ and is chosen to be a hundred times higher than the 'natural' roughness in order to ensure a sufficiently large amplitude of the control mode. Note that the roughness elements are modelled by inhomogeneous wall boundary conditions (cf. equation 5.1). Two DNS solutions are presented, one where only the "natural" roughness is considered and a second one with both the "natural" and the control roughness. The latter solution is presented in figure 7.2. The wavy structures that become apparent and their tendency to 'roll over' are clear indicators of strong steady crossflow instabilities. Similar structures have been identified in experiments by Reibert et al. (1996) and Saric et al. (1998a). The structures which are visible in the first spanwise plane shown in figure 7.2 are quite even and regular

 $^{^1\}mathrm{The}$ DNS was performed by Solmaz Akbaripour Sheijnai as part of a Master thesis

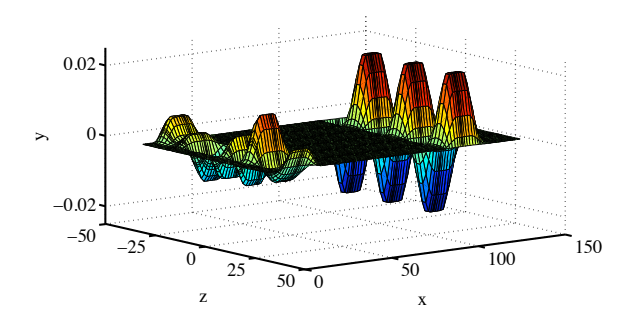


FIGURE 7.1. Two spanwise arrays of roughness elements are shown. The first is used to excite multiple steady crossflow disturbances with wavenumbers $k\beta_0$ with k=1,2,...,6 and $\beta_0=0.1$. The second array represents the 'control' roughness the height of which is scaled by a factor of 0.1 for visualisation purposes. The spanwise wavenumber is chosen as $\beta=3\beta_0$.

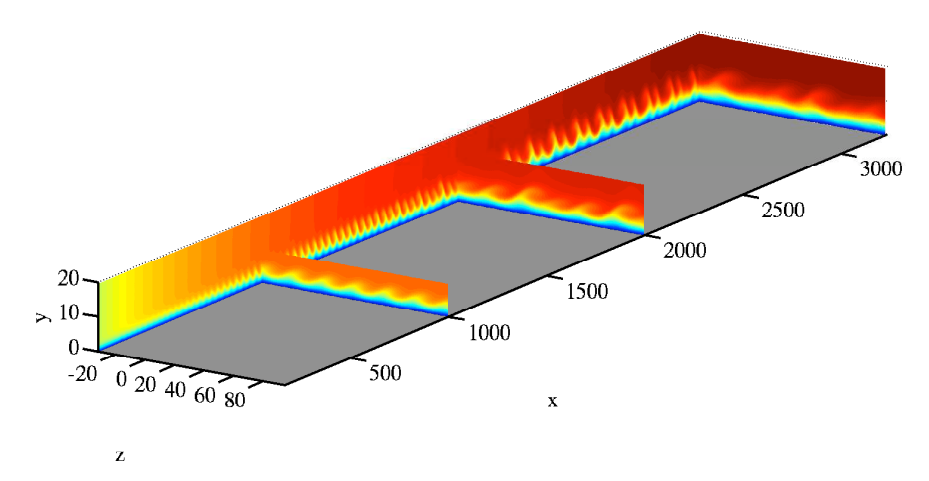
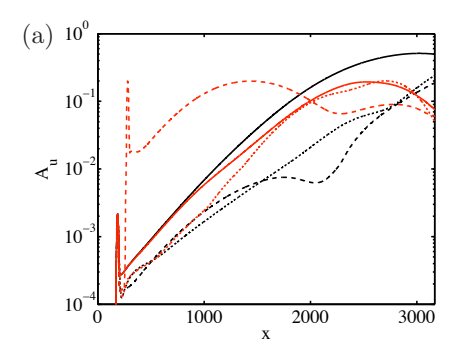


FIGURE 7.2. Total velocity component (U+u') of the controlled case. The steady disturbances are excited by the roughness elements shown in figure 7.1.

and thus denote the dominance of one single crossflow mode. However, farther downstream a competition of several disturbance modes becomes apparent.

In order to identify the dominant modes and to illuminate the effect of the control roughness as compared with the uncontrolled case amplitudes of the individual crossflow modes are extracted by means of a Fast Fourier transformation with respect to the spanwise direction. It is apparent from figure 7.3 that the target mode chosen above represents the naturally most unstable wave



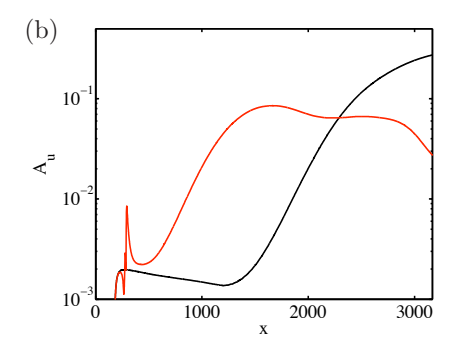


FIGURE 7.3. (a) Amplitudes of the fundamental (\cdots) , target (-) and control (--) mode in the uncontrolled (black lines) and the controlled case (red lines). (b) Amplitude of the meanflow distortion in the uncontrolled (-) and controlled case (-).

since it dominates the uncontrolled case. Towards the end of the computational domain nonlinear effects lead to an amplitude saturation of the target mode which, under natural conditions, would quickly lead to the onset of secondary instabilities and to a breakdown to turbulent flow. This picture is principally different in the controlled case. Initially the control mode dominates the disturbance field exhibiting amplitudes which are almost two orders of magnitude larger than those of all other modes. For x > 1000 it becomes stable and decays. However, due to its large initial amplitude it has, through nonlinear interactions, affected the target mode in a favourable way as is apparent in figure 7.3(a). Compared to the uncontrolled case the target mode gets attenuated for x > 750. Towards the end of the domain it even decays resulting in an amplitude difference of about one order of magnitude as compared to the uncontrolled case. This effect is explained by the so-called meanflow distortion. The large initial amplitude of the control mode leads to early nonlinear interactions that significantly affect the meanflow (cf. figure 7.3 b). Figure 7.4 shows that this distortion leads to a meanflow which exhibits fuller profiles in the near-wall region as compared to the undisturbed and uncontrolled cases for x < 2200. Further, the distortion reduces the crossflow and consequently stabilises crossflow disturbances. Both these observations resemble effects of wall suction on the meanflow profiles which is known to stabilise the boundary layer (cf. Wassermann & Kloker 2002). To conclude, this example has shown that triggering subcritical forcing can be efficiently used to stabilise a threedimensional boundary layer with respect to stationary crossflow disturbances. However, when applying this technique for transition control, also the effect on secondary, non-stationary instabilities needs to be considered. This is discussed in paper 5.

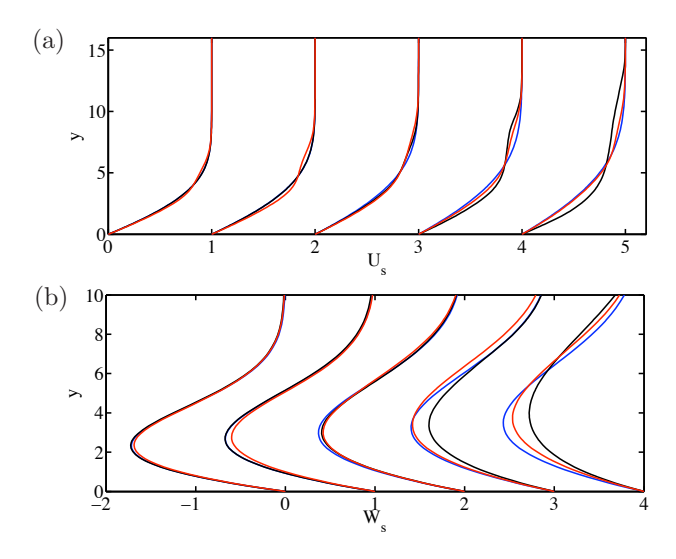


FIGURE 7.4. Profiles of the undisturbed baseflow (—), the uncontrolled (—) and the controlled (—) case. From left to right the profiles are extracted at x=1167,1667,2167,2667,3167 and are shifted along the x-axes for visualisation purposes. (a) Profiles of the streamwise velocity (b) Profiles of the crossflow velocity

CHAPTER 8

Summary & Conclusions

The work presented in this thesis focuses on the study of receptivity mechanisms in three-dimensional, crossflow-dominated boundary layers. Two model problems, a swept-flat-plate and a swept-wing boundary layer are considered. Furthermore, tools are presented and evaluated that allow to efficiently study and predict both receptivity and stability of boundary-layer flows.

The PSE, which have been extensively employed throughout this work, represent one such tool. Because of their parabolic nature they can be solved very efficiently by simple marching techniques. A modification of the classical PSE has been presented herein for crossflow-dominated boundary layers, which allows for the study of more general and, in particular, non-modal disturbances. In combination with their adjoint, the PSE have been used to determine optimal initial disturbances as well as to predict receptivity to both surface roughness and vortical disturbances. Results for swept-flat-plate boundary layers demonstrate a significant potential for non-modal growth in three-dimensional boundary layers. Optimal disturbances take the form of streamwise vortices initially and experience extensive spatial growth even in regions where the flow is stable with respect to modal disturbances. As optimal disturbances turn into crossflow modes farther downstream, non-modal growth may be related to a receptivity mechanism in crossflow-dominated boundary layers. By comparing to respective DNS results, the adjoint-based PSE have been found to yield excellent predictions of swept-wing boundary layer receptivity to micron-sized surface roughness.

Direct numerical simulations of the LNSE, though much more costly than solving the PSE, provide another means to study receptivity mechanisms. While the PSE are restricted to slowly varying shear flows such as boundary layers on simple geometries, DNS may be performed for complex configurations and strongly non-parallel flows. Within the linear framework receptivity can be studied by combining the solutions of the direct LNSE and its adjoint. This approach is efficient in the sense that only two simulations, *i.e.* one direct and one adjoint, are required to predict the receptivity amplitude of a certain boundary-layer disturbance excited by any external disturbance environment. In particular, it becomes possible to determine boundary-layer receptivity to incoming free-stream disturbances upstream of the leading edge. This ultimately allows to predict boundary-layer receptivity to free-stream turbulence provided that the turbulent velocity field in the homogeneous free-stream is

known. Herein, direct and adjoint solutions of the LNSE for a swept-wing boundary layer are used to determine worst-case scenarios which lead to maximum receptivity amplitudes in the linear sense. Both the worst-case surface roughness and the worst-case free-stream disturbance are presented. It is shown that, under such optimal conditions, swept-wing boundary layers are more receptive to surface roughness than to incoming free-stream disturbances.

Furthermore, receptivity predictions on the basis of the PSE and DNS have been compared to experimental results by Reibert et al. (1996). These authors studied the excitation of crossflow disturbances by localised surface roughness in a swept-wing boundary layer. The PSE and DNS results are in perfect agreement. Although the predicted amplitudes are slightly below those measured in the experiments, the overall agreement with experimental results is very satisfactory. The stabilisation of the same boundary layer by localised roughness elements is demonstrated by means of DNS. The results confirm experiments by Saric et al. (1998a) and show that transition may be completely suppressed.

Most models for transition prediction which are in use today disregard the receptivity process. Such semi-empirical models, rely on correlations of disturbance growth with experimentally determined transition locations. However, it is known that crossflow-dominated boundary layers exhibit a distinct dependence on the external disturbance environment. A robust transition prediction therefore has to account for the receptivity process which determines the initial conditions of the boundary layer disturbances. The receptivity tools that are presented in this thesis might be combined with other efficient methodologies, such as the nonlinear PSE, which accurately predict the linear and nonlinear growth of primary disturbances. The predicted flow state may then be used as an input for secondary instability analyses. A correlation based on secondary instabilities was shown to yield accurate and robust transition predictions (cf. Malik et al. 1999). Hence, a combination of the presented tools with secondary instability analysis has the potential for efficient and robust transition prediction.

CHAPTER 9

Acknowledgements

I want to express my gratitude to Ardeshir Hanifi and Dan Henningson for their guidance and generous support and for giving me a lot of freedom. I want to thank Dan, who initially was my main supervisor, for many valuable ideas and for always taking his time to discuss research matters. I am very grateful to Ardeshir, who later took over as my main advisor, for his dedication and for being a great teacher.

Many people at KTH Mechanics have contributed to a productive and very pleasant atmosphere over the past few years. In particular, I want to thank my close and long-time PhD colleagues Lars-Uve Schrader, Antonios Monokrousos, Johan Malm, Onofrio Semeraro, Qiang Li and Lailai Zhu for countless helpful discussions and for being really good friends. I am very grateful to Luca Brandt and Philipp Schlatter for always providing help when needed. Thanks to Armin Hosseini for the fruitful collaboration during my last year as well as to Thomas Kurian for the co-operation during my first three years and for enjoyable trips to project meetings across Europe. Paul Fischer is gratefully acknowledged for his support with the 'Nek5000' code.

I want to thank all current and former group members, *i.e.* Shervin, Espen, Yohann, Milos, Stefan I., Sasan, Reza, Azad, Gaetano, Iman, Mattias, Nima, Ruth and Karl as well as Andreas V., Andreas C., Enrico, Amin, Zeinab, Florian, Peter, Marit, Stevin, Outi, Bengt, Gabriele, Ramis, Hanno, Erik, Henrik, Arne, Nicholas, Geert, Fredrik, Jens, Carolina, Heide, Malin, Bubba and many others at the department for creating such a friendly atmosphere.

Partial financial support by the European Commission through the FP6 project 'TELFONA' (Contract No AST4-CT-2005-516109) is gratefully acknowledged.

Many thanks to our friends here in Stockholm and especially to Simon and Anna who have been the key for a very pleasant life besides work. Deepest gratitude I feel for my parents and my entire family for their great support over all these years.

Sarah, thank you for your love and support. Your contribution to this thesis is invaluable! Finally, thank you Meja for all your charming smiles and for bringing so much happiness and excitement into our lives.

Bibliography

- AIRIAU, C. 2000 Non-parallel acoustic receptivity of a Blasius boundary layer using an adjoint approach. Flow Turbul. Combust. 65, 347–367.
- ÅKERVIK, E., EHRENSTEIN, U., GALLAIRE, F. & HENNINGSON, D. S. 2008 Global two-dimensional stability measures of the flat plate boundary layer flow. *Eur. J. Mech B/Fluids* **27**, 501–513.
- Amoignon, O., Pralits, J., Hanifi, A., Berggren, M. & Henningson, D. 2006 Shape optimization for delay of laminar-turbulent transition. AIAA J. 45 (5), 1009-1024.
- Andersson, P., Berggren, M. B. & Henningson, D. S. 1999 Optimal disturbances and bypass transition in boundary layers. *Phys. Fluids* 11, 134–150.
- Andersson, P., Henningson, D. & Hanifi, A. 1998 On a stabilization procedure for the parabolic stability equations. *J. Engng Math.* **33** (3), 311–332.
- Arnal, D. & Casalis, G. 2000 Laminar-turbulent transition prediction in three-dimensional flows. *Progr. Aerosp. Sci.* **36**, 173–191.
- ASHPIS, D. E. & RESHOTKO, E. 1990 The vibrating ribbon problem revisited. *J. Fluid Mech.* **213**, 531–547.
- BERTOLOTTI, F. P. 1991 Linear and nonlinear stability of boundary layers with streamwise varying properties. PhD thesis, Ohio State University.
- BERTOLOTTI, F. P. 2000 Receptivity of three-dimensional boundary-layers to localized wall roughness and suction. *Phys. Fluids* **12** (7), 1799–1809.
- Bertolotti, F. P., Herbert, T. & Spalart, P. R. 1992 Linear and nonlinear stability of the blasius boundary layer. *J. Fluid Mech.* **242**, 441–474.
- BIPPES, H. 1999 Basic experiments on transition in three-dimensional boundary layers dominated by crossflow instability. *Progr. Aerosp. Sci.* **35**, 363–412.
- BOTTARO, A. 2010 A receptive boundary layer. J. Fluid Mech. 646, 1-4.
- Brandt, L., Schlatter, P. & Henningson, D. 2004 Transition in boundary layers subject to free-stream turbulence. *J. Fluid Mech.* **517**, 167–198.
- COOKE, J. C. 1950 The boundary layer of a class of infinite yawed cylinders. *Proc. Camb. Phil. Soc.* **46**, 645–648.
- CORBETT, P. & BOTTARO, A. 2001 Optimal linear growth in swept boundary layers. J. Fluid Mech. 435, 1–23.
- CROUCH, J. D. 1993 Receptivity of three-dimensional boundary layers. AIAA Paper 93-0074 .
- DEYHLE, H. & BIPPES, H. 1996 Disturbance growth in an unstable three-dimensional

- boundary layer and its depence on environmental conditions. J. Fluid Mech. 316, 73–113
- Dobrinsky, A. 2002 Adjoint analysis for receptivity prediction. PhD thesis, Rice University.
- Dobrinsky, A. & Collis, S. S. 2000 Adjoint parabolized stability equations for receptivity prediction. AIAA Paper 2000-2651 .
- Falkner, V. M. & Skan, S. W. 1931 Solutions of the boundary layer equation. *Phil. Mag.* 12, 865–896.
- Fedorov, A. V. 1988 Excitation of waves of instability of the secondary flow in the boundary layer on a swept wing. J. Appl. Mech. Tech. Physics, 643–648.
- FISCHER, P. F., LOTTES, J. W. & KERKEMEIER, S. G. 2008 nek5000 Web page. Http://nek5000.mcs.anl.gov.
- GIANNETTI, F. & LUCHINI, P. 2006 Leading-edge receptivity by adjoint methods. J. Fluid Mech. 547, 21–53.
- GREGORY, N., STUART, J. T. & WALKER, W. S. 1955 On the stability of three-dimensional boundary layers with applications to the flow due to a rotating disk. *Philos. Trans. R. Soc. London Ser. A* 248, 155–99.
- GROSCH, C. E. & SALWEN, H. 1978 The continuous spectrum of the Orr-Sommerfeld equation. Part 1. The spectrum and the eigenfunctions. J. Fluid Mech. 87, 33–54.
- HAJ-HARIRI, H. 1994 Characteristics analysis of the parabolized stability equations. Stud. Appl. Math. 92, 41–53.
- HALL, P. 1985 The Görtler vortex instability mechanism in three-dimensional boundary layers. Proc. R. Soc. London A 399, 135–152.
- Hall, P., Malik, M. R. & Poll, D. I. A. 1984 On the stability of an infinite swept attachment-line boundary layer. *Proc. R. Soc. London A* 395, 229–45.
- HANIFI, A., HENNINGSON, D. S., HEIN, S., BERTOLOTTI, F.P. & SIMEN, M. 1994 Linear non-local instability analysis - the linear NOLOT code. FFA TN 1994-54.
- Hein, S., Hanifi, A. & Casalis, G. 2000 Nonlinear transition prediction. In Proceedings of the European Congress on Computational Methods in Applied Sciences and Engineering.
- HERBERT, T. 1993 Studies of boundary-layer receptivity with parabolized stability equations. AIAA Paper 93-3053.
- HERBERT, T. 1994 Parabolized stability equations. In AGARD Report 793, Special course on progress in transition modelling, 4/1–3/34.
- HERBERT, T. 1997 Parabolized stability equations. Annu. Rev. Fluid Mech. 29, 245–283.
- HILL, D. C. 1995 Adjoint systems and their role in the receptivity problem for boundary layers. J. Fluid Mech. 292, 183–204.
- Hill, D. C. 1997 Receptivity in non-parallel boundary layers. In *Proceedings of the* 1997 ASME Fluids Engineering Division Summer Meeting. ASME.
- HÖGBERG, M. & HENNINGSON, D. 1998 Secondary instability of cross-flow vortices in Falkner-Skan-Cooke boundary layers. J. Fluid Mech. 368, 339–357.
- JACOBS, R. G. & DURBIN, P. A. 2001 Simulations of bypass transition. J. Fluid Mech. 428, 185–212.
- KLEBANOFF, P. S. 1971 Effect of free-stream turbulence on the laminar boundary layer. *Bull. Am. Phys. Soc.* 10, 1323.

- Kurian, T., Fransson, J. H. M. & Alfredsson, P. H. 2011 Boundary layer receptivity to free-stream turbulence and surface roughness over a swept flat plate. *Phys. Fluids* 23, 034107.
- LANDAHL, M. T. 1980 A note on algebraic instability of inviscid parallel shear flows. J. Fluid Mech. 98, 243–251.
- LI, F. & MALIK, M. 1996 On the nature of the PSE approximation. Theoret. Comput. Fluid Dyn. 8, 253–273.
- LI, F. & Malik, M. 1997 Spectral analysis of parabolized stability equations. Comp. Fluids 26 (3), 279–297.
- LIN, N., STUCKERT, G. & HERBERT, T. 1995 Boundary layer receptivity to freestream vortical disturbances. AIAA Paper 95-0772 .
- LIN, R. & Malik, M. R. 1996 On the stability of attachment-line boundary layers. Part 1. The incompressible swept Hiemenz flow. *J. Fluid Mech.* **311**, 239–255.
- LUCHINI, P. 2000 Reynolds-number-independent instability of the boundary layer over a flat surface: optimal perturbations. J. Fluid Mech. 404, 289–309.
- Luchini, P. & Bottaro, A. 1998 Görtler vortices: a backward-in-time approach to the receptivity problem. J. Fluid Mech. 363, 1–23.
- Mack, C. J., Schmid, P. J. & Sesterhenn, J. L. 2008 Global stability of swept flow around a parabolic body: connecting attachment-line and crossflow modes. *J. Fluid Mech.* **611**, 205–214.
- MACK, L. M. 1984 Boundary-layer linear stability theory. In AGARD Report 709, Special course on stability and transition of laminar flow, 3/1–3/81.
- Malik, M. R., Li, F., Choudhari, M. M. & Chang, C.-L. 1999 Secondary instability of crossflow vortices and swept-wing boundary-layer transition. *J. Fluid Mech.* **399**, 85–115.
- MESSING, R. & KLOKER, M. 2010 Investigation of suction for laminar flow control of three-dimensional boundary layers. J. Fluid Mech. 658, 117–147.
- ORR, W. M. F. 1907 The stability or instability of the steady motions of a liquid. *Proc. R. Irish Acad.* A 27, 9–69.
- Patera, A. T. 1984 A spectral element method for fluid dynamics: laminar flow in a channel expansion. *J. Comp. Phys.* **54**, 468–488.
- Pralits, J. O., Airiau, C., Hanifi, A. & Henningson, D. S. 2000 Sensitivity analysis using adjoint parabolized stability equations for compressible flows. *Flow Turbul. Combust.* **65**, 321–346.
- Pralits, J. O. & Hanifi, A. 2003 Optimization of steady suction for disturbance control on infinite swept wings. *Phys. Fluids* **15** (9), 2756–2772.
- RADEZTSKY, R. H., REIBERT, M. S. & SARIC, W. S. 1999 Effect of isolated micronsized roughness on transition in swept-wing flows. AIAA J. 37 (11), 1370–1377.
- RAYLEIGH, L. 1880 On the stability of certain fluid motions. *Proc. Math. Soc. Lond.* 11, 57–70.
- Reibert, M. S. 1996 Nonlinear stability, saturation, and transition in crossflow-dominated boundary layers. PhD thesis, Arizona State University.
- Reibert, M. S., Saric, W. S., Carillo, R. B. & Chapman, K. L. 1996 Experiments in nonlinear saturation of stationary crossflow vortices in a swept-wing boundary layer. *AIAA Paper 96-0184*.
- Salwen, H. & Grosch, C. E. 1981 The continuous spectrum of the Orr-Sommerfeld equation. Part 2. Eigenfunction expansions. *J. Fluid Mech.* **104**, 445–465.

- SARIC, W. S. 1994 Görtler vortices. Annu. Rev. Fluid Mech. 26, 379-409.
- SARIC, W. S., CARILLO, R. B. & REIBERT, M. S. 1998a Leading-edge roughness as a transition control mechanism. AIAA Paper 98-0781 .
- SARIC, W. S., CARILLO, R. B. & REIBERT, M. S. 1998b Nonlinear stability and transition in 3-D boundary layers. *Meccanica* 33, 469–487.
- SARIC, W. S., REED, H. L. & WHITE, E. B. 2003 Stability and transition of three-dimensional boundary layers. *Annu. Rev. Fluid Mech.* **35**, 413–440.
- Schlichting, H. 1933 Zur Entstehung der Turbulenz bei der Plattenströmung. Nachr. Ges. Wiss. Göttingen, Math. Phys. Klasse,, 171–174.
- SCHLICHTING, H. 1979 Boundary-Layer Theory, seventh edn. McGraw-Hill.
- SCHMID, P. J. 2007 Nonmodal stability theory. Annu. Rev. Fluid Mech. 39, 129–162.
- Schmid, P. J. & Henningson, D. S. 2001 Stability and Transition in Shear Flows. Springer.
- Schrader, L. U., Amin, S. & Brandt, L. 2010 Transition to turbulence in the boundary layer over a smooth and rough swept plate exposed to free-stream turbulence. *J. Fluid Mech.* **646**.
- Schrader, L. U., Brandt, L. & Henningson, D. S. 2009 Receptivity mechanisms in three-dimensional boundary layer flows. J. Fluid Mech. 618, 209–241.
- Schubauer, G. B. & Skramstad, H. K. 1947 Laminar boundary layer oscillations and stability of laminar flow. J. Aero. Sci. 14, 69–78.
- Simen, M. 1992 Local and non-local stability theory of spatially varying flows. In *Instability, Transition and Turbulence*, 181–195. Springer Verlag.
- Somers, D. M. & Horstmann, K.-H. 1985 Design of a medium-speed, natural laminar-flow airfoil for commuter aircraft applications. *DLR-IB* **129-85/26**.
- TEMPELMANN, D. 2009 Stability and receptivity of three-dimensional boundary layers. TRITA-MEK 2009:19, Licentiate thesis, KTH Stockholm.
- Tempelmann, D., Hanifi, A. & Henningson, D. S. 2010 Optimal disturbances and receptivity in three-dimensional boundary layers. In *Proceedings of the 5th European Conference on Computational Fluid Dynamics ECCOMAS CFD* (ed. J. C. F. Pereira & A. Sequeira).
- Tempelmann, D., Schrader, L.-U., Hanifi, A., Brandt, L. & Henningson, D. S. 2011 Numerical study of boundary-layer receptivity on a swept wing. AIAA Paper 2011-3294.
- Theofilis, V. 2011 Global linear instability. Annu. Rev. Fluid Mech. 43, 319–52.
- Theofilis, V., Barkley, D. & Sherwin, S. 2002 Spectral/hp element technology for global flow instability and control. *Aeronaut. J.* **106**, 619–625.
- Tollmen, W. 1929 Über die Entstehung der Turbulenz 1. Mitteilung. Nachr. Ges. Wiss. Göttingen, Math. Phys. Klasse, 21–44.
- Trefethen, L. N., Trefethen, A. E., Reddy, S. C. & Driscoll, T. 1993 Hydrodynamic stability without eigenvalues. *Science* **261**, 578–584.
- Tumin, A. 2003 Multimode decomposition of spatially growing perturbations in a two-dimensional boundary layer. *Phys. Fluids* **15** (9), 2525–2540.
- Tumin, A. & Reshotko, E. 2001 Spatial theory of optimal disturbances in boundary layers. *Phys. Fluids* **13** (7), 2097–2104.
- Wassermann, P. & Kloker, M. 2002 Mechanics and passive control of crossflow-vortex-induced transition in a three-dimensional boundary layer. *J. Fluid Mech.* **456**, 49–84.

- Wassermann, P. & Kloker, M. 2003 Transition mechanisms induced by travelling crossflow vortices in a three-dimensional boundary layer. *J. Fluid Mech.* 483, 67–89
- Weideman, J. A. & Reddy, S. C. 2000 A Matlab differentiation matrix suite. $ACM\ Trans.\ Math.\ Softw.\ (TOMS)\ {\bf 26}\ (4).$
- White, E. B. & Saric, W. S. 2005 Secondary instability of crossflow vortices. $\it J. Fluid Mech. 525, 275-308.$

Part II

Papers